International Journal of Plasticity 170 (2023) 103770

Contents lists available at ScienceDirect

International Journal of Plasticity

journal homepage: www.elsevier.com/locate/ijplas

Negative stacking fault energy in FCC materials-Its implications

Daegun You, Orcun Koray Celebi, Ahmed Sameer Khan Mohammed,
Huseyin Sehitoglu [*]

Department of Mechanical Science and Engineering, University of Illinois at Urbana-Champaign, 1206 W. Green St., Urbana, IL 61801, USA

ARTICLE INFO

Keywords:
Stacking fault
Critical stress
Dislocations
Wigner-Seitz cell

ABSTRACT

Recent atomistic simulations on medium entropy alloys uncovered the possibility of negative intrinsic stacking fault energies (SFEs), which suggest infinite stacking fault widths (SFWs). However, experimental measurements of SFWs in the same alloys have shown that SFWs are finite, which contradicts the classical derivations based on force balance. To address this contradiction, we develop an advanced treatment employing atomistic lattice and continuum theories that produce finite SFW solutions corresponding to negative SFEs. The idea is based on energy minimization, where the finite SFW corresponds to the first local minimum in the energy landscape. By exploring combinations of intrinsic and unstable fault energies, we identify regimes in which solutions for finite SFWs exist for thousands of hypothetical materials. Elastic moduli and lattice constants also impact the results, with lower moduli and smaller lattice constants expanding the negative stacking fault energy domain corresponding to finite SFWs. Additionally, the study has revealed a distribution of SFEs due to possible chemical heterogeneities within the alloy, resulting in variations in SFWs within the same material. The work underscores the capabilities of the theory for SFW and CRSS (Critical Resolved Shear Stress) determination for medium to high entropy alloys in agreement with experiments.

1. Introduction

A stacking fault (SF) is a planar defect that exists between two split partial dislocations and is characterized by the stacking fault energy (SFE) (Vítek, 1968). The separation distance between the two partials, i.e., the stacking fault width (SFW), is ideally determined from the balance between forces from elastic repulsion and planar misfit (attraction) of the two partials. The lower the intrinsic SFE (γ_{isf}), the higher the SFW. The unstable SFE (γ_{us}) represents the highest energy barrier of the Generalized Stacking Fault Energy (GSFE) landscape. The higher the barriers γ_{us}, the higher the Critical Resolved Shear Stress (CRSS) (Joós and Duesbery, 1997) and the smaller the dislocation core-width. This background has been well-established in the materials science (Chowdhury and Sehitoglu, 2017a, 2017b; Nabarro, 1967; Ogata et al., 2002; Phillips, 2001; Tadmor and Miller, 2011). In addition, the energy landscape also influences the dislocation motion in deformation-induced twinning and martensitic transformation (Alkan and Sehitoglu, 2019; Alkan et al., 2018b; Chowdhury and Sehitoglu, 2017a, 2017b; Kibey et al., 2007; Wang and Sehitoglu, 2013) and constitutes the bedrock of materials science and mechanics. We draw attention to modifications to the above treatment that captures a strong dependence of CRSS on the dislocation character (screw, edge, and mixed) affected by the elastic energies and the Wigner-Seitz cell describing the correct periodicity at the crystal level (Celebi et al., 2023; Mohammed et al., 2022). Such a treatment unraveled the correct flow

---

[*] Corresponding author.
E-mail address: huseyin@illinois.edu (H. Sehitoglu).

https://doi.org/10.1016/j.ijplas.2023.103770
Received 29 June 2023; Received in revised form 13 September 2023;
Available online 5 October 2023

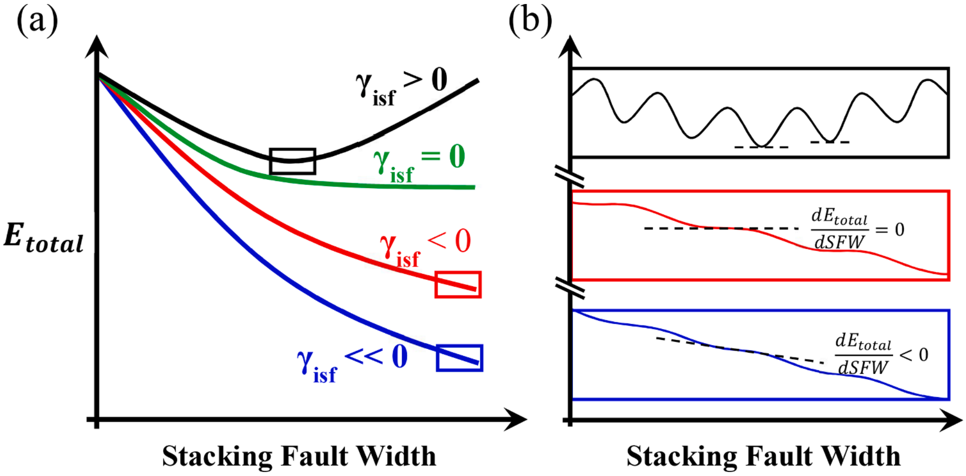

Fig. 1. A schematic of total energy variation upon stacking fault width (SFW; or the separation distance between Shockley partial dislocations). (a) Total energy E_{total} is the sum of the elastic interaction energy around the dislocations and the misfit energy in a lattice. The scenarios are divided into positive, zero, negative, and largely negative intrinsic stacking fault energy (γ_{isf}). (b) A schematic of E_{total} curves based on the Wigner-Seitz (WS) cell-based misfit energy. The WS cell-based misfit energy characterizes multiple local Peierls valleys that can determine the finite SFW upon intermittent motion of partials. In each case, the derivatives $\frac{dE_{total}}{dSFW}$ are denoted as dashed lines.

resistance (as CRSS) for dislocations of mixed character.

In summary, in the case of a positive value for γ_{isf}, there is a textbook understanding of how the energetics are balanced for partial dissociation (Read, 1953). The elastically isotropic interaction between two partials and the SFE portion stretched by the equilibrium SFW are energetically balanced together. This classical relation between SFW and γ_{isf} based on the assumption of isotropic FCC materials is,

$$SFW = \frac{G\, b_p^2}{8\pi\, \gamma_{isf}} \left(\frac{2-\nu}{1-\nu}\right)\left(1 - \frac{2\nu\, \cos(2\theta)}{2-\nu}\right) \tag{1}$$

where G is shear modulus, b_p the magnitude of a partial Burgers vector, ν Poisson's ratio, and θ the angle between the full Burgers vector and its dislocation line.

Now, we turn our attention to recent atomistic simulations that showed the negative SFEs in several alloys, but measurements show a finite SFW. In earlier treatments, the γ_{isf} has been inferred from SFW measurements as potentially positive (Laplanche et al., 2017). Nevertheless, the above classical formula cannot be defined at zero and should not be applied to negative SFE values. The negative γ_{isf} has been theoretically found in high nitrogen steels (Kibey et al., 2006) and medium or high entropy alloys (MHEAs) (Huang et al., 2018; Li et al., 2022; Niu et al., 2018; Zhang et al., 2017a, 2017b; Zhao et al., 2017). Still, the results show finite SFWs in the experiments (Laplanche et al., 2017; Liu et al., 2018, 2019; Okamoto et al., 2016; Picak et al., 2019; Wang et al., 2018b; Wei and Tasan, 2020; Zaddach et al., 2013; Zhang et al., 2020). This issue presents an anomaly. Also, the classical conversion formula does not show dependency on the entire energy landscape and is uncoupled from the dislocation core-widths and anisotropic elastic energy. Therefore, the relationship can be applied only to positive SFE values as emphasized in numerous textbooks (Hirth and Lothe, 1992; Hull and Bacon, 2001; Read, 1953). This paper proposes a solution to this seeming contradiction with a new theory. We describe our approach next.

In Fig. 1a, the typical curves for total energy E_{total} are plotted with respect to the SFW for the positive, zero, and negative γ_{isf} cases. As two Shockley partials are dissociated, the elastic interaction between two partials produces a repulsive force, which is reduced as the SFW increases. The positive γ_{isf} produces an attractive force opposing the elastic interaction. Then, the global equilibrium SFW can be found by balancing the elastic interaction and positive misfit energy for the positive γ_{isf}. However, the global minimum cannot be defined for the negative γ_{isf} as the elastic and misfit energies both decrease with increasing the SFW. For the $\gamma_{isf} = 0$ case, although the misfit energy tends to stay constant with increasing separation distance, the elastic energy decreases due to the repulsive force between the partials, and therefore will not yield a global minimum for the total energy E_{total}.

Recently, the ab-initio/anisotropic elasticity framework, developed as Mohammed et al. (2022) (abbreviated as MCS) model, has formulated the total energy for the motion of Shockley partials, including the Wigner-Seitz (WS) cell-based misfit energy in the crystal lattice. It resulted in the correct determination of the CRSS, SFW, and core structures of Shockley partial dislocations. It was validated for numerous metals and alloys (You et al., 2023) and with different dislocation characters (Celebi et al., 2023). In Fig. 1b, the total energy E_{total} can be characterized by fluctuations based on the Peierls valleys, which dictate the intermittent zig-zag motion of partials. Therefore, for the positive γ_{isf}, the finite SFW is derived for the local and global minima (a derivative of E_{total}, $\frac{dE_{total}}{dSFW} = 0$). For the negative γ_{isf} in general, there is no global minimum energetic point (global equilibrium SFW). However, E_{total} exhibits multiple local

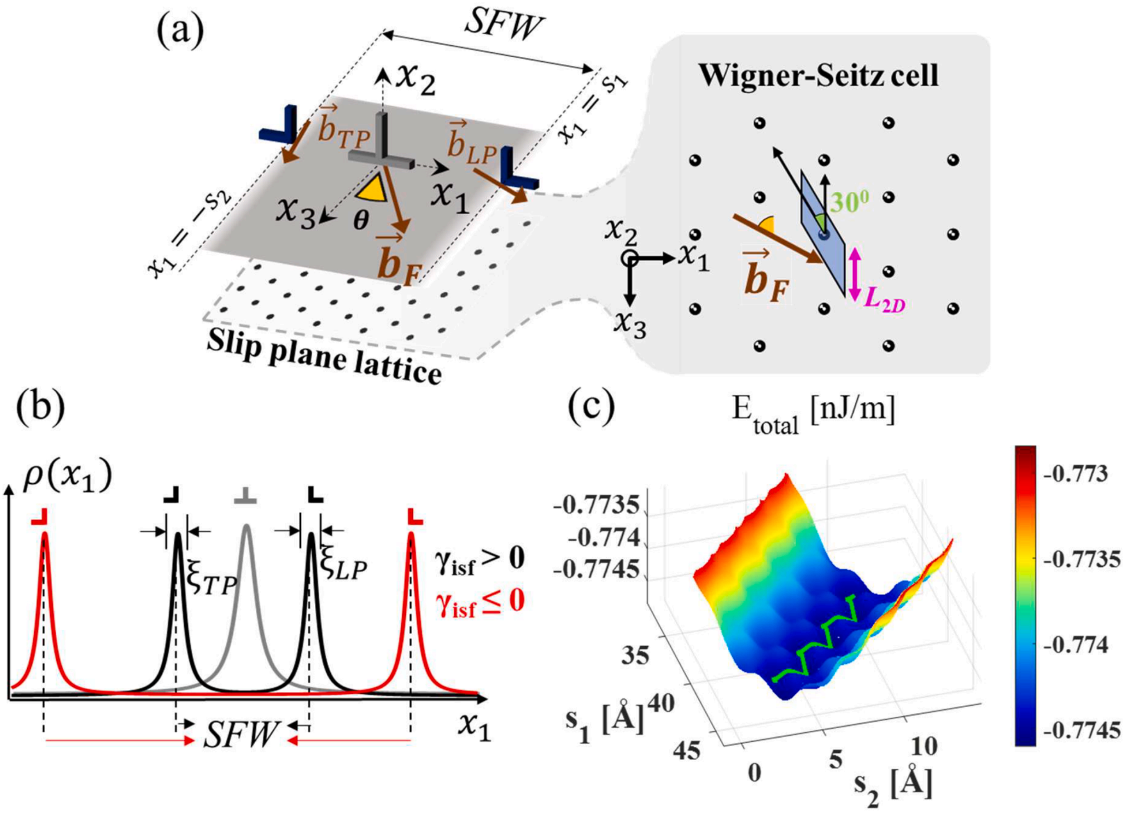

Fig. 2. (a) Schematic of the extended dislocation and Wigner-Seitz (WS) cell-based misfit energy; For a given core structure of an extended dislocation in FCC materials with a full Burgers vector ($\vec{b}_F = a/2[\overline{11}0]$) on a $(1\bar{1}1)$ plane, $\vec{b}_{LP} = a/6[\overline{121}]$ is the one for a leading partial (LP), and $\vec{b}_{TP} = a/6[\overline{21}1]$ for a trailing partial (TP). L_{2D} is the normalization length in the repeated dislocation lines. $\vec{b}_F$ can be screw, edge, or mixed character with an angle of θ. Two Shockley partials are separated by stacking fault width (SFW); The LP is at position $x_1 = s_1$ and the TP is at $x_1 = -s_2$, yielding the SFW as $s_1 + s_2$. (b) The plot of the dislocation-density distribution $\rho(x_1)$; A density of full dislocation is colored as gray, and two cases for partial dislocations are black and red, where γ_{isf} is either positive and negative, indicating the core-widths ξ_{TP} and ξ_{LP}, respectively; As $\gamma_{isf} \leq 0$, partial dislocations are freely moving. (c) Minimum energy path (MEP) result of Shockley partials is shown with the zig-zag motion; Stacking fault energies, $\gamma_{us} = 300$ mJ/m^2 and $\gamma_{isf} = 20$ mJ/m^2, are used to demonstrate a typical example of the previous framework.

minima corresponding to finite SFW. The first minimum is the smallest possible SFW, but this does not preclude the existence of multiple metastable minima. In fact, this is consistent with other experimental observations that usually have a large variation of the SFWs in the FCC materials (Laplanche et al., 2017; Liu et al., 2018, 2019; Okamoto et al., 2016; Picak et al., 2019; Wang et al., 2018b; Wei and Tasan, 2020; Zaddach et al., 2013; Zhang et al., 2020), which may have the negative γ_{isf}. Recent approaches have attempted to explain this discrepancy by proposing the existence of a frictional barrier bounding the stacking-fault width for negative γ_{isf} materials (Lu et al., 2023; Sun et al., 2021; Werner et al., 2023, 2021).

In this work, we numerically demonstrate a novel ab-initio framework extending the MCS model into the negative γ_{isf} criterion described above. For the partial dislocation motion with negative γ_{isf}, we consider the local minimum concept of E_{total} and the critical stress to further dissociate the partials in the framework. These are consistent with experimental variations in the SFWs and CRSS. Based on the results, we explain how the critical negative γ_{isf} (γ_{cisf}) can be determined, which provides a stable regime of multiple finite SFW. Then, we mainly illustrate the following new findings; (1) Stability regimes that map out non-zero solutions for the finite SFWs in FCC materials by correlating γ_{us} and γ_{isf}; (2) Effects of lattice constant (a), and elastic moduli (C_{11}, C_{12}, and C_{44}) on the stability maps; (3) SFW contours; and (4) CRSS and core-widths. All the results of (3) and (4) are defined in the stability maps, including both γ_{us} and γ_{isf}. We finally predict and benchmark the characteristics of the well-known MHEA to validate the framework with their experimental results.

2. Methods

2.1. Analytical framework

The current analytical framework is based on the notion of energy minimization utilizing the Wigner-Seitz (WS) cell-area on the slip plane to establish the dislocation core-width and partial dislocation separation. Fig. 2 represents the typical schematic and results based on the previous framework suggested by Mohammed et al. (2022) (abbreviated as MCS). It has the originality of combining the anisotropic elastic interaction, the WS cell-based atomistic misfit energy, and the energy-minimization of intermittent motion of Shockley partial dislocations in FCC materials. In Fig. 2a, the core structure of an extended dislocation is depicted. As slip occurs, the separated partials have a repulsive elastic interaction. At the same time, the WS cell-based misfit energy in a crystal lattice produces an attractive force and balances the elastic component. The total energy is a minimum at a finite separation distance. In the given coordinate system and a dislocation character (the angle between full Burgers vector $\vec{b}_F$ and the dislocation line), Burgers vectors (full $\vec{b}_F$, leading $\vec{b}_{LP}$, and trailing partial $\vec{b}_{TP}$) can be correspondingly defined. Instead, we consider the fixed Burgers vectors as the references of the extended dislocation and vary the global coordinate system that corresponds to the dislocation character. In this work, we demonstrate the framework mainly based on a screw character with different material constants such as lattice constant a, elastic moduli C_{11}, C_{12}, C_{44}, fault energy barriers γ_{us}, and γ_{isf}. The global coordinate system for the screw character is defined as $\vec{e}_1 \| [1\overline{1}\overline{2}]$, $\vec{e}_2 \| [1\overline{1}1]$, and $\vec{e}_3 \| [\overline{1}\overline{1}0]$.

In Fig. 2b, the dislocation-density distribution $\rho(x_1)$ is plotted. As a slip is introduced, the density of a full dislocation becomes separated into two components for Shockley partials, including the leading (LP) and trailing partials (TP) indicating the core-widths ξ_{LP} and ξ_{TP}, respectively. The distance between two partials is then characterized by the SFW. The $\rho(x_1)$ for two cases are represented as black and red, where γ_{isf} is either positive or negative. As we conceptually design the idea for the negative γ_{isf}, the dissociation of $\rho(x_1)$ can be largely defined or separated continuously. We first demonstrate the previous framework defined in the positive γ_{isf}, and finally extend it into the negative region in Section 2.3. The dislocation-density distributions are derived from the core disregistry functions, $f(x_1)$, of the LP and TP. Both the core disregistry distributions $f(x_1)$ and dislocation-density distributions $\rho(x_1)$ for the partial Burgers vectors are defined as the following equations:

$$f_{LP}(x_1) = \frac{b_p}{2} + \frac{b_p}{\pi}\tan^{-1}\left(\frac{x_1 - s_1}{\xi_{LP}}\right);\ \rho_{LP}(x_1) = \frac{b_P}{\pi}\left(\frac{\xi_{LP}}{(x_1 - s_1)^2 + \xi_{LP}^2}\right) \tag{2}$$

$$f_{TP}(x_1) = \frac{b_p}{2} + \frac{b_p}{\pi}\tan^{-1}\left(\frac{x_1 + s_2}{\xi_{TP}}\right);\ \rho_{TP}(x_1) = \frac{b_P}{\pi}\left(\frac{\xi_{TP}}{(x_1 + s_2)^2 + \xi_{TP}^2}\right) \tag{3}$$

where b_p is the magnitude of the partial Burgers vector, and s_1, s_2 are the positions of LP and TP respectively, which determines that SFW $= s_1 + s_2$. Eqs. (2) and (3) explicitly represent the several key parameters of the core structures in the extended dislocation, such as the core-width ξ_{LP}, ξ_{TP}, and the SFW based on the positions of partials. In the previous studies on the MCS framework, the core structure parameters are determined upon minimization of total energy (E_{total}) of the extended dislocation in FCC crystals, as E_{total} is composed of two energy components,

$$E_{total}(\xi_{LP}, \xi_{TP},\ s_1, s_2) = E_{strain}(\xi_{LP}, \xi_{TP},\ s_1, s_2) + E_{misfit}(\xi_{LP}, \xi_{TP},\ s_1, s_2) \tag{4}$$

where E_{strain} is the elastic strain-energy based on the anisotropic Eshelby-Stroh (E-S) formalism (Barnett and Lothe, 1974; Stroh, 1958), and E_{misfit} is the misfit energy utilizing the equivalent WS cell-area in the crystal lattice. For the details of the elastic strain-energy and misfit energy formalism, the reader may refer to elsewhere (Mohammed et al., 2022).

The strain-energy component $E_{strain}(\xi_{LP}, \xi_{TP},\ s_1, s_2)$ for the extended dislocation can be calculated from the anisotropic interaction coefficients on each Shockley partial. $E_{strain}(\xi_{LP}, \xi_{TP},\ s_1, s_2)$ consists of the self-interaction energies of the LP and TP (such as $E^{11}_{elastic}$ and $E^{22}_{elastic}$, respectively) and the interaction energy between the two partials ($E^{12}_{elastic}$). Therefore, $E_{strain}(\xi_{LP}, \xi_{TP},\ s_1, s_2)$ is expressed as

$$E_{strain}(\xi_{LP}, \xi_{TP},\ s_1, s_2) = E^{11}_{elastic} + E^{22}_{elastic} + E^{12}_{elastic} \tag{5}$$

All terms on the right-hand side are summed up with the elastic interaction energy between infinitesimal fractional dislocations derived from the cores of the partials, and they are defined as follow,

$$\begin{aligned} E^{11}_{elastic} &= \int_{-\infty}^{\infty}\int_{-\infty}^{\infty}\left(\frac{K_{11}}{2\pi}\right)\rho_{LP}(x)\rho_{LP}(y)\ln|x-y|dxdy \\ E^{22}_{elastic} &= \int_{-\infty}^{\infty}\int_{-\infty}^{\infty}\left(\frac{K_{22}}{2\pi}\right)\rho_{TP}(x)\rho_{TP}(y)\ln|x-y|dxdy \\ E^{12}_{elastic} &= \int_{-\infty}^{\infty}\int_{-\infty}^{\infty}\left(\frac{K_{12}}{2\pi}\right)\rho_{LP}(x)\rho_{TP}(y)\left(\vec{b}_{LP}.\vec{b}_{TP}\right)\ln|x-y|dxdy \end{aligned} \tag{6}$$

where K_{11}, K_{22}, and K_{12} are the anisotropic interaction coefficients to be computed, and x and y are arbitrary variables defined in x_1-axis in Fig. 2b. As an example, the procedure to determine K_{12} can be briefly explained. We can consider the LP and TP separated by a certain distance R. The continuum strain-fields surrounding each Shockley partial are determined and superposed based on the E-S formalism to determine the net strain-field. The strain-energy density is then numerically integrated to calculate the total strain-energy of interaction at the chosen separation distance R, and a core region within radius $5b_p$ around the center of each partial is excluded. By calculating the total strain-energy at varying R, the interaction coefficient K_{12} is determined. The choice of $5b_p$ does not affect K_{12} calculation since the gradient of change of total strain-energy is conserved. Therefore, there is no effect of singularity in our theory, although one may apply the non-singular formulation (Cai et al., 2006) instead and investigate this aspect in different studies. The self-interaction coefficients K_{11} and K_{22} can be similarly determined by considering the interaction between two dislocations with the same Burgers vectors. For a more detailed exposition of anisotropic interaction coefficients and the E-S formalism, the reader is referred to elsewhere (Mohammed et al., 2022).

For the formulation of the WS cell-based misfit energy $E_{misfit}(\xi_{LP},\xi_{TP},\ s_1,s_2)$, the generalized stacking fault energy (GSFE) curve is required for each LP and TP. The GSFE curves for the LP and TP are defined as:

$$\gamma_{LP}(u) = \begin{cases} \gamma_{isf} + \left(\dfrac{\gamma_{us} - \gamma_{isf}}{2}\right)\left(1 - \cos\left(\dfrac{2\pi u}{b_P}\right)\right) \text{ for } 0 \le u \le \dfrac{b_P}{2} \\ \dfrac{\gamma_{us}}{2}\left(1 - \cos\left(\dfrac{2\pi u}{b_P}\right)\right) \text{ for } \dfrac{b_P}{2} \le u \le b_P \end{cases} \tag{7}$$

$$\gamma_{TP}(u) = \begin{cases} \dfrac{\gamma_{us}}{2}\left(1 - \cos\left(\dfrac{2\pi u}{b_P}\right)\right) \text{ for } 0 \le u \le \dfrac{b_P}{2} \\ \gamma_{isf} + \left(\dfrac{\gamma_{us} - \gamma_{isf}}{2}\right)\left(1 - \cos\left(\dfrac{2\pi u}{b_P}\right)\right) \text{ for } \dfrac{b_P}{2} \le u \le b_P \end{cases} \tag{8}$$

where γ_{us} and γ_{isf} are unstable and intrinsic stacking fault energies, respectively. Based on Eqs. (2), (3), and (7), (8), the E_{misfit} can be rewritten with the partitioned GSFE into the WS cell area for the individual Shockley partials,

$$E_{misfit}(\xi_{LP},\xi_{TP},\ s_1,s_2) = \frac{1}{L_{2D}}\left[\begin{array}{c} \displaystyle\sum_{n=-N_0}^{N_0}\sum_{m=-M_{max}}^{-1}\gamma_{TP}\left(f_{TP}\left(x_1^{(m,n)}\right)\right)\Delta A \\ \displaystyle \ldots\ldots + \sum_{n=-N_0}^{N_0}\sum_{m=0}^{M_{max}}\gamma_{LP}\left(f_{LP}\left(x_1^{(m,n)}\right)\right)\Delta A \end{array}\right] \tag{9}$$

where $x_1^{(m,n)} = (m\overrightarrow{a}_1 + n\overrightarrow{a}_2)\cdot\overrightarrow{e}_1$, ΔA is the area of the WS cell, and L_{2D} is the normalization length in the repeated dislocation lines. A summation limit of M_{max} is chosen with a large number, of the order of 10^4, to sufficiently converge the $E_{misfit}(\xi_{LP},\xi_{TP},\ s_1,s_2)$. The misfit energy in Eq. (9) is calculated per unit length of the dislocation line. For the positive γ_{isf}, four parameters $(\xi_{LP},\xi_{TP},\ s_1,s_2)$ are consequently determined by the Eq. (4) with respect to the equilibrium core structure $(\xi_{LP}^0,\ \xi_{TP}^0,s_1^0,s_2^0)$ at the global minimum of E_{total} in such that

$$\frac{\partial E_{total}}{\partial \xi_{LP}} = 0;\ \frac{\partial E_{total}}{\partial \xi_{TP}} = 0;\ \frac{\partial E_{total}}{\partial s_1} = 0;\ \frac{\partial E_{total}}{\partial s_2} = 0 \tag{10}$$

The minimization routine is implemented with *fmincon* in MATLAB. Details for the dependence of each energy component on the core parameters are found in the previous studies (Celebi et al., 2023; Mohammed et al., 2022).

2.2. Minimum energy path (MEP) of partial dislocations and CRSS

The previous MCS framework formulated the minimum energy path (MEP) with the equilibrium core-widths $(\xi_{LP}^0,\ \xi_{TP}^0)$ to find the triangular trajectory that allows the robust intermittent movement of Shockley partials (Mohammed et al., 2022; You et al., 2023), which is energetically more favorable than the case where the partials move together with a constant separation width. The positions of Shockley partials (s_1,s_2) are described by the following equations along with the triangular trajectory,

$$\begin{aligned} s_1 &= s_1^0 + \frac{1}{\sqrt{2}}\left(t + \sum_{k=1}^{n} C_k\left(1 - P\left(C_p,j\right)\right)\right) \\ s_2 &= s_2^0 + \frac{1}{\sqrt{2}}\left(-t + \sum_{k=1}^{n} C_k\left(1 - P\left(C_p,j\right)\right)\right) \end{aligned} \tag{11}$$

where t is a path variable to parametrize the trajectory. $P(C_p,j)$ is the triangular pulse generator and j is a pulse-variable defined as follows,

$$j = \frac{t}{C_q} + C_p - \left\lfloor \frac{t}{C_q} + C_p \right\rfloor \tag{12}$$

$$P\left(C_p, j\right) = \begin{cases} 0 & \text{for } j \leq 0 \\ \dfrac{j}{C_p} & \text{for } 0 < j < C_p \\ \dfrac{1-j}{1-C_p} & \text{for } C_p < j < 1 \\ 0 & \text{for } j \geq 1 \end{cases} \tag{13}$$

where the lower bracket of $\lfloor x \rfloor$ is a floor function $\lfloor x \rfloor. = \max\{X \in \mathbb{Z} : X \leq x\}$, and the parameter combination $(C_1, \ldots, C_n, C_p, C_q)$ defines a shape for a triangular path of positions of Shockley partials. The total energy cumulated along with the triangular trajectory given in Eq. (11) is accordingly defined as the following objective function,

$$E_{path}\left(C_1, \ldots, C_n, C_p, C_q\right) = \sum_i E_{total}\left(s_1(t_i), s_2(t_i), \xi_{LP}^0,\ \xi_{TP}^0\ \right) \tag{14}$$

The number of periodic functions is simply set to $n = 1$ sufficient to capture the MEP. The roles of path parameters such as t and (C_1, C_p, C_q) can be also understood with the equilibrium point found at $t = 0$ for (s_1^0, s_2^0) and the positive γ_{isf} with $C_1\ = 0$, which is the amplitude of triangular path. C_p and C_q are a peak position and a period of the triangular path, respectively. The triangular pulse generator $P(C_p, j)$ is implemented with *triangularPulse* in MATLAB. The equilibrium parameters $(\xi_{LP}^0,\ \xi_{TP}^0, s_1^0, s_2^0)$ for the case of positive γ_{isf} are employed along with the triangular trajectory described by Eq. (11), and the minimization routine in Eq. (14) is also implemented with *fmincon* and multiple initial points (*MultiStart*) in MATLAB to find the corresponding MEP.

In the conventional Peierls-Nabarro (PN) model (Joós and Duesbery, 1997; Nabarro, 1947; Peierls, 1940), the CRSS has been calculated by taking only the simple misfit energy based on the one-dimensional cubic row-summation. Thus, it is expressed as,

$$CRSS_{PN} = \max\left(\frac{1}{b_F}\frac{dE_{misfit}^{PN}}{du}\right) \tag{15}$$

where b_F is the magnitude of the full dislocation, $E_{misfit}^{PN}(u)\ = \sum_{m=-\infty}^{\infty}\gamma(f(ma^{'}\ - u))a^{'}$, γ is the GSFE curve, f is the disregistry function given by equation x, and $a^{'}$ is interplanar spacing perpendicular to the dislocation line, respectively. The MCS framework suggested the optimum-energy-trajectory (OET) approach for the CRSS prediction that resolved the limitations in the PN model such as (i) the motion of individual Shockley partials with a constant SFW, (ii) the dependency of CRSS on the full Burgers vector b_F only, not on the partial Burgers vector b_p, and (iii) the one-dimensional simple-cubic row-summation misfit-energy. For more detailed coverage of the OET approach and its derivation, readers are referred to the original work (Mohammed et al., 2022). Based on the OET approach, the CRSS is defined as,

$$CRSS_{MCS} = SF_F \cdot \max\left(\frac{1}{(SF_{LP}\cdot s_1^{'}(t) - SF_{TP}\cdot s_2^{'}(t))}\frac{1}{b_p}\frac{dE_{total}}{dt}\right) \tag{16}$$

where b_p is the magnitude of the Burgers vector in Shockley partials, $SF_F\ = (\vec{v}\cdot\vec{n}_{slip})(\vec{v}\cdot\vec{b}_F)$, $SF_{LP}\ = (\vec{v}\cdot\vec{n}_{slip})(\vec{v}\cdot\vec{b}_{LP})$, and $SF_{TP} = (\vec{v}\cdot\vec{n}_{slip})(\vec{v}\cdot\vec{b}_{TP})$ are Schmid Factors (*SF*s) resolved in the full extended dislocation, LP, and TP, $\vec{v}$ is the unit vector along the uniaxial tensile load direction $[1\overline{3}2]$, and $\vec{n}_{slip} = 1/\sqrt{3}[1\overline{1}1]$ the normal vector to the slip plane, respectively. The CRSS in Eq. (16) appears different than the conventional PN approach in Eq. (15) where a single partial is solely considered, since the OET approach in this work includes partial separation trajectory.

In Fig. 2c, a typical result is shown with the MCS framework for the positive γ_{isf} in a screw character. The material parameters are set as $a = 3.6$ Å, $C_{11} = 221$ GPa, $C_{12} = 152$ GPa, $C_{44} = 165$ GPa, $\gamma_{us} = 300$ mJ/m^2, and $\gamma_{isf} = 20$ mJ/m^2. In the total energy contour along with the positions of Shockley partials (s_1, s_2), the optimized MEP (green line) is represented. Based on the minimization in Eq. (10), the equilibrium core-widths $(\xi_{LP}^0,\ \xi_{TP}^0)$ of Shockley partials yield both $\xi_{LP}^0 = \xi_{TP}^0 = 3.20$ Å, and their equilibrium positions (s_1^0, s_2^0) are (40.5 Å, 7.42 Å), which results in the global equilibrium SFW, $SFW_0 = 47.9$ Å. Then, the CRSS of the given input parameters finally yields the CRSS $= 11.0$ MPa based on Eq. (16), at the maximum derivative of total energy, which is resolved in its OET. The fluctuation in the SFW, $SFW\ = SFW_0 + \Delta SFW$, is due to the intermittent zig-zag motion of Shockley partials, and its magnitude ΔSFW for the present case is 1.91 Å which is dictated by the six material parameters.

2.3. Extension of framework into non-positive γ_{isf} regime

As described in Sections 2.1 and 2.2, the MCS framework determines the global minimum of total energy E_{total} in the extended dislocation of FCC crystals. For non-positive γ_{isf}, however, the global minimum of E_{total} based on four parameters $(\xi_{LP}, \xi_{TP},\ s_1, s_2)$ cannot be defined since the anisotropic E_{strain} is continuously reduced and the WS cell-based E_{misfit} component stays constant ($\gamma_{isf} = 0$) or decreases ($\gamma_{isf} < 0$) with fluctuations as the SFW increases. Previous studies found that medium and high entropy alloys (MHEAs) exhibiting negative γ_{isf} (Huang et al., 2018; Li et al., 2022; Niu et al., 2018; Zhang et al., 2017a, 2017b; Zhao et al., 2017) demonstrate a

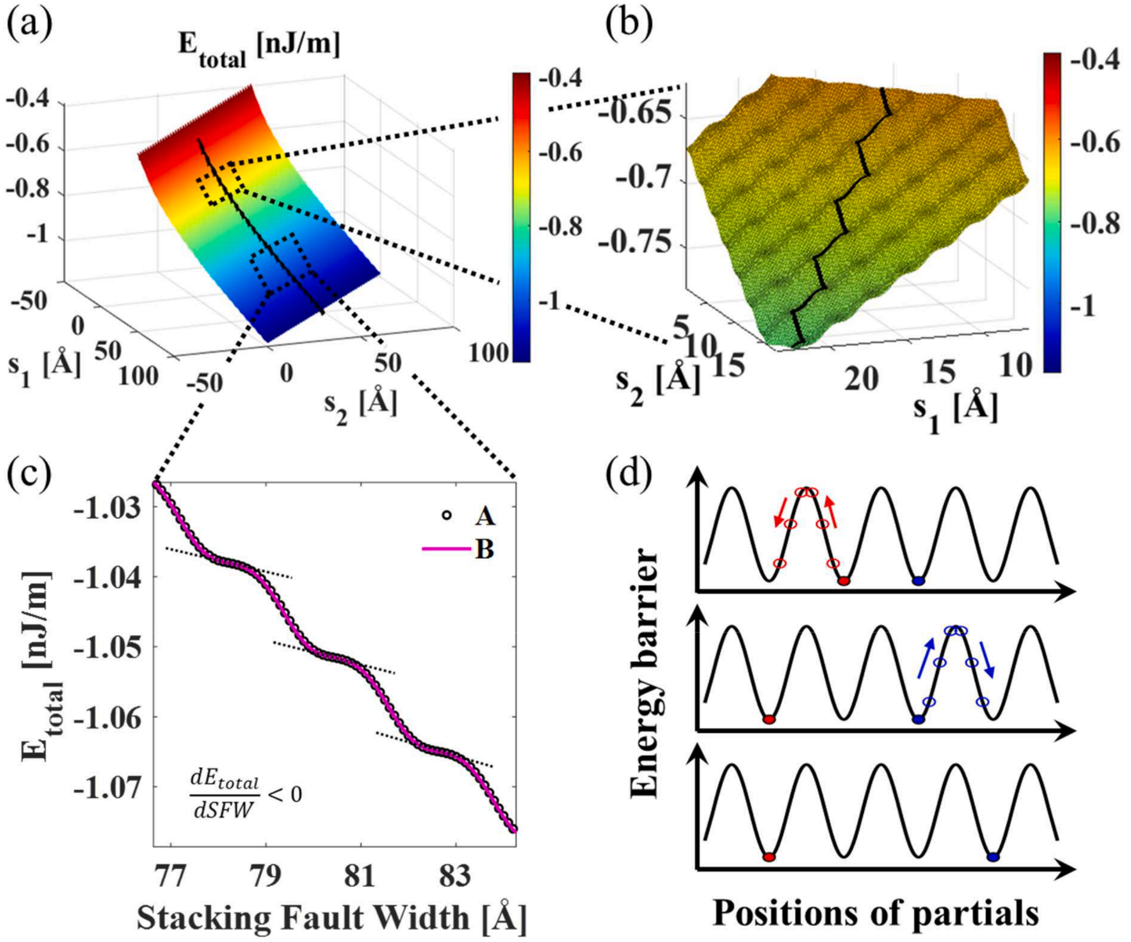

Fig. 3. Freely extending motions of dislocations and their energetics with largely negative stacking fault energy. (a) Total energy landscape of screw dislocation in the space of the positions (s_1, s_2) of Shockley partials; The minimum energy path (MEP) is denoted as a black solid line. (b) Enlarged view of total energy surface plot to see a zig-zag motion of partials in free dissociation. (c) The same energetics from two different MEP solutions A (black circle) and B (purple line) in the SFW scale, $SFW = s_1 + s_2$; A is an intermittent zig-zag motion of Shockley partials, and B is the isolated motion with one of Shockley partials fixed (TP in this case). (d) A schematic of energy barrier upon varying positions of Shockley partials; One is denoted as red, and the other as blue. Material constants used in this case are $a = 3.6$ Å, $\mu = 34.5$ GPa, $C_{44} = 165$ GPa, $\gamma_{us} = 439$ mJ/m^2, and $\gamma_{isf} = -50$ mJ/m^2, respectively.

significant variation in SFWs, as observed in experimental measurements (Laplanche et al., 2017; Liu et al., 2018, 2019; Okamoto et al., 2016; Picak et al., 2019; Wang et al., 2018b; Wei and Tasan, 2020; Zaddach et al., 2013; Zhang et al., 2020). Therefore, in these materials, the Shockley partial dislocations can be effectively modeled as being consistently separated from one another. In other words, as $\gamma_{isf} \leq 0$, partial dislocations are freely moving until any positive valleys on the fluctuations of E_{total}, which can be equivalently evaluated if the derivative of E_{total} (or dissociation stress) becomes positive or not. Therefore, in this section, (i) we firstly make the triangular trajectory start from the closely zero SFW, (ii) numerically show how E_{total} and its derivative vary with respect to the SFW, and (iii) finally demonstrate the determination of a critical negative γ_{isf} (γ_{cisf}) to achieve finite SFW and CRSS.

The triangular trajectory defined in Eq. (11) can be expressed as follows,

$$\begin{aligned} s_1 &= s_1^{in} + \frac{1}{\sqrt{2}}\left(t + \sum_{k=1}^{n} C_k\left(1 - P\left(C_p, j\right)\right)\right) \\ s_2 &= s_2^{in} + \frac{1}{\sqrt{2}}\left(t + \sum_{k=1}^{n} C_k\left(1 - P\left(C_p, j\right)\right)\right) \end{aligned} \tag{17}$$

where s_1^{in} and s_2^{in} are the initial positions of Shockley partials that are to be specified. It is ideal that s_1^{in} and s_2^{in} are set to zero in order to investigate E_{total} versus the SFW, although two core structures of partials are overlapped at the small SFW region. Therefore, the minimum threshold of SFW$_{in}$ is set as $SFW_{in} = s_1^{in} + s_2^{in} > 2\xi_P$. The change of sign convention in the path variable t in s_2 is intended to

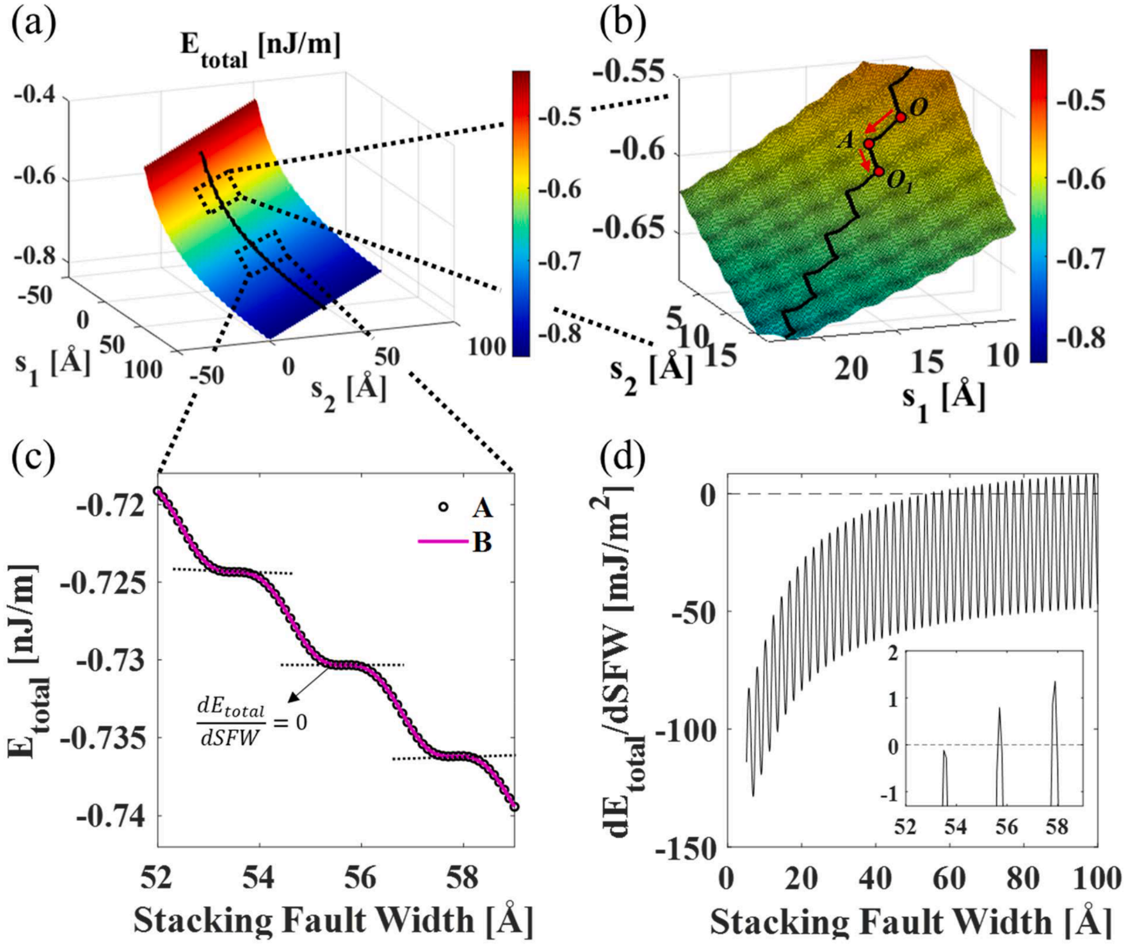

Fig. 4. Freely extending motions of dislocations and their energetics with slightly negative stacking fault energy. (a) Total energy landscape of screw dislocation in the space of the positions (s_1, s_2) of Shockley partials; The MEP is denoted as a black solid line; (b) Enlarged view of total energy surface plot to see a zig-zag motion of partials in free dissociation. Shockley partials traverse the minimum-energy path (MEP) including the points *O, A*, and *O₁*; (c) Equivalent energies from two different MEP solutions A and B; The LP is fixed for the solution B of the isolated motion; (d) Plot of derivative of total energy with respect to the SFW $= s_1 + s_2$, in the given SFW range up to 100 Å. Material constants used in this case are $a = 3.559$ Å, $\mu = 45.2$ GPa, $C_{44} = 138.4$ GPa, $\gamma_{\text{us}} = 418$ mJ/m^2, and $\gamma_{\text{isf}} = -10$ mJ/m^2, respectively.

model the motion of partials to be continuously dissociated. In arbitrary shapes of the triangular trajectory in the specified range of $SFW = s_1 + s_2$, two parameters (ξ_{LP}, ξ_{TP}) can be iteratively determined at each set of values in s_1 and s_2 based on the Eq. (4) with respect to the equilibrium core structure (ξ_{LP}^0, ξ_{TP}^0) at the minimum of E_{total} in such that

$$\frac{\partial E_{total}}{\partial \xi_{LP}} = 0; \quad \frac{\partial E_{total}}{\partial \xi_{TP}} = 0 \tag{18}$$

Then, the outer loop searching for the MEP is implemented with Eq. (14) by changing the shape of the triangular trajectory.

Fig. 3 demonstrates an example of freely extending motions of Shockley partial dislocations based on Eqs. (17) and (18). The material constants needed for total energy calculation are referred to the one of HEAs (NiCoCrFeMn) with are $a = 3.6$ Å, $\mu = (C_{11} - C_{12})/2 = 34.5$ GPa, $C_{44} = 165$ GPa, $\gamma_{\text{us}} = 439$ mJ/m^2, and $\gamma_{\text{isf}} = 8$ mJ/m^2 (Alkan et al., 2018a). Based on this input set, we investigate E_{total} variation with the SFW by hypothetically changing γ_{isf} into the negative side. Hence, we can determine a base point of γ_{isf}, i.e. the critical value γ_{cisf}, for the given combination of the input set. Initially, γ_{isf} is set to be -50 mJ/m^2, and s_1^{in} and s_2^{in} are 6 Å and 0 Å, which SFW_{in} becomes 6 Å. The range of the $SFW = s_1 + s_2$ to be calculated is set up to 100 Å. In Fig. 3a, E_{total} surface is depicted in the space of the positions (s_1, s_2) of Shockley partial dislocations. The one of the MEPs is determined in the loop over Eq. (14) and denoted as a black solid line. As shown in Fig. 3b, the MEP passes through the minimum valleys, as E_{total} keeps decreasing. It is comparably different from the positive γ_{isf} case described in Fig. 2c, which has a global valley in E_{total}.

In Fig. 3c, E_{total} is depicted along the MEP trajectory in the SFW axis by $SFW = s_1 + s_2$. Also, another solution (B) of the MEP is compared to the zig-zag trajectory (A). The solution B includes only one Shockley partial moving and the other being fixed at s_1^{in} or s_2^{in}.

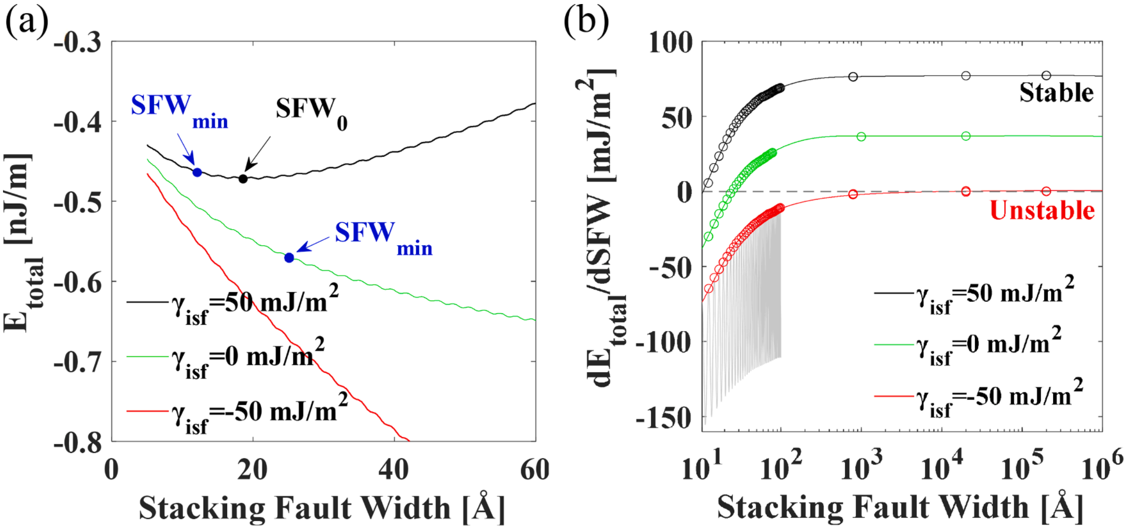

Fig. 5. Total energies and dissociation stresses in screw dislocation upon the variation of SFW with various γ_{isf} cases; (a) Plot of total energy in the vicinity of the SFW for the global minimum (SFW_0) and the first local minimum (SFW_{min}). SFW_0 for the zero or negative γ_{isf} is not defined; (b) Convergence of peak in the derivatives of total energy at high SFW. Critical intrinsic stacking fault energy (γ_{cisf}) is determined as closely at $\gamma_{isf} = -50$ mJ/m^2. Gray curve represents the fluctuations in the derivative of total energy for $\gamma_{isf} = -50$ mJ/m^2; Material constants are $a = 3.6$ Å, $\mu = 34.5$ GPa, $C_{44} = 165$ GPa, $\gamma_{us} = 439$ mJ/m^2. The minimum threshold of SFW is given as SFW > $2\xi_P$.

Therefore, the MEP for the negative γ_{isf} in the screw character has four equivalent solutions at the same initial values. As an example, we show the solution B (isolated motion) for the TP being fixed at $s_2^{in} = 0$ Å, and find that the solution A and B have the same energetics. It can be also explained by the energy barrier needed for each Shockley partial to move, as shown in Fig. 3d as the schematic of the solution A. It describes that one partial dislocation (red) moves away, while the other (blue) is fixed. Then, the latter one starts to move in the same situation. In the perspective of continuous dissociation, either LP or TP moving cannot be distinguished. Likewise, the energetics of the solution B is also not distinguishable from the solution A. In Fig. 3c, we also find no positive derivative of E_{total} with respect to the SFW, i.e., $\frac{dE_{total}}{dSFW} < 0$, in the given range up to 100 Å. The main idea of this work is that the negative γ_{isf} contributes two partials to be continuously separated until E_{total} reaches its local minimum. Hence, in the given material constant set with γ_{isf} modulated to -50 mJ/m^2, two partials will continue the dissociation beyond the SFW range of 100 Å.

Fig. 4 demonstrates another example of freely extending motions of Shockley partial dislocations, but based on the slightly negative γ_{isf}. The material constants used in this case are referred to the one of MEAs (NiCoCr) with are $a = 3.559$ Å (Huang et al., 2018), $\mu = (C_{11} - C_{12})/2 = 45.2$ GPa, $C_{44} = 138.4$ GPa (Laplanche et al., 2020). In this case, however, we modulate both SFEs (γ_{us}, γ_{isf}), since not all material constants are compatibly paired within the consistencies in MD or experiments. We here set $\gamma_{us} = 418$ mJ/m^2, and $\gamma_{isf} = -10$ mJ/m^2. The γ_{isf} is chosen as a slightly negative value in the previous studies (Alkan et al., 2018a; Celebi et al., 2022; Chandran and Sondhi, 2011; Datta et al., 2009; Ding et al., 2018; Huang et al., 2018; LaRosa and Ghazisaeidi, 2022; Li et al., 2022; Niu et al., 2018; Shang et al., 2012; Siegel, 2005; Sun et al., 2021; Tian et al., 2017; Wang et al., 2018a; Zhang and Wang, 2022; Zhang et al., 2017a, 2017b; Zhao et al., 2019, 2017), which are tabulated in **Table S1** in Supplementary Material. Based on the parameter set, we also investigate E_{total} variation with the SFW by hypothetically changing both γ_{us} and γ_{isf} into the negative γ_{isf} side. The initial values such as s_1^{in}, s_2^{in}, SFW_{in}, and the range of SFW are also set to 6 Å, 0 Å, 6 Å, and 6–100 Å, respectively, as the same as the case in Fig. 3. In Fig. 4a, E_{total} surface is depicted in the space of the positions (s_1, s_2) of Shockley partial dislocations. The one of the MEPs as a zig-zag solution A is also determined. In Fig. 4b, the MEP in this case also passes through the minimum valleys well, such as O, A, and O_1 as indicated. In Fig. 4c, E_{total} is depicted along the MEP trajectory in the SFW axis, and the solution B also shows the equivalent energetics. Here, the solution B has the LP fixed at $s_1^{in} = 0$ Å, and we note that the solution B (isolated motion) is computationally more efficient than the solution A. Therefore, all further results after the demonstration are implemented by using the solution B.

In Fig. 4c, we find a transition point from negative to positive derivative of E_{total} in the given range 6–100 Å. This is described well with the derivative curve as shown in Fig. 4d. The fluctuations in $\frac{dE_{total}}{dSFW}$ stem from the variations in E_{total} including Peierls valleys, which are based on the WS cell-based misfit energy. Among the multiple local minima, we find the first intersection of $\frac{dE_{total}}{dSFW}$ to initial zero dissociation stress at SFW = 55.5 Å. Therefore, the MEA NiCoCr with the given material constant set can have a least finite SFW at this point, since it starts to require positive stress for partials to continue the dissociation. Also, the MEA NiCoCr is reported to have multiple SFW varying 39.6 Å to 72.5 Å (56.3 Å on average) in the screw character ($\theta < \sim 3^\circ$) (Laplanche et al., 2017; Liu et al., 2018; Shih et al., 2021), which agrees well with the calculation in this work. Nevertheless, if the external stress is continuously introduced at a higher level than the dissociation stress, the statement that two partials keep separating still holds, as a large variation of the SFW is shown in experiments. Therefore, we finally investigate the maximum dissociation stress by further extending partial separation.

Fig. 5 represents the total energies and their dissociation stresses upon changing the SFW with modulating γ_{isf} in three scenarios such as positive $\gamma_{isf} = +50$ mJ/m^2, zero $\gamma_{isf} = 0$, and negative $\gamma_{isf} = -50$ mJ/m^2. In Fig. 5a, E_{total} is depicted in the narrow range where its local or global minimum can be defined in each case. In the case of zero or negative γ_{isf}, the global minimum cannot be defined since the strain-energy is continuously reduced and the WS cell-based misfit energy stays constant or decreases with its oscillation. Only the positive γ_{isf} (+50 mJ/m^2) determines the global minimum of E_{total} at its SFW denoted as the SFW₀ (18.6 Å). Also, the positive γ_{isf} (+50 mJ/m^2) introduces the multiple local minima including the global one. It can be easily identified with the multiple intersections in the dissociation stress $\frac{dE_{total}}{dSFW}$ as similarly seen in Fig. 4d. Among the multiple minima, E_{total} at its first local one is denoted with the SFW$_{\min}$ (12.1 Å) where non-zero external stress is initially required to dissociate the partials. For the zero γ_{isf}, it has also multiple local minima, and the SFW$_{\min}$ is measured as 25.4 Å. However, there is no local minimum found for the negative γ_{isf} (−50 mJ/m^2) in the given window.

In Fig. 5b, we extend the dissociation into an infinitely large domain up to 2×10^5 Å. The dissociation stress $\frac{dE_{total}}{dSFW}$ for the negative γ_{isf} (−50 mJ/m^2) closely intersects with zero at infinitely large SFW, as compared to other cases $\gamma_{isf} = 0$ or $+ 50$ mJ/m^2. The intersections and flucuations are described in Fig. A1 in Appendix A. It implies that all $\gamma_{isf} \leq -50$ mJ/m^2 will result in the non-positive dissociation stress for any SFW, and therefore those types of materials will be unstable with respect to the dissociation. These materials hypothetically continue their dissociation of partial dislocations without external stress. It can be deduced that they may stand no longer belong to the FCC structure, since the continuous dissociation mechanism will accordingly create a deformation-induced phase transformation. The negative γ_{isf} (−50 mJ/m^2) is therefore determined as the critical negative value γ_{cisf} for the given material constants ($a = 3.6$ Å, $\mu = 34.5$ GPa, $C_{44} = 165$ GPa, and $\gamma_{us} = 439$ mJ/m^2). For $\gamma_{isf} > \gamma_{cisf}$, a positive external stress is required to further dissociate the partials beyond the first local minimum (SFW$_{\min}$). Here we define the maximum dissociation stress $\frac{dE_{total}}{dSFW}$ as the CRSS in FCC materials with the negative γ_{isf}. The maximum derivative of E_{total} is resolved in the one of MEPs as the same as the positive γ_{isf} case. In either case of the solution A or B, the OET approach is still applicable based on Eq. (16). In Fig. 4b for the solution A, we have $s_1'(t) > 0$ and $s_2'(t) = 0$ in the segment OA, given the MEP beginning at point O. In section AO_1, similarly, we have $s_1'(t) = 0$ and $s_2'(t) > 0$. In other words, along the trajectory, there is an intermittent motion of the Shockley partials where in any given segment (OA or AO_1) only one partial is moving. Considering the segment OA, the gradient of SFW is given by,

$$\frac{dSFW}{dt} = s_1'(t) + s_2'(t) = s_1'(t) \tag{19}$$

$$CRSS_{MCS} = SF_F \cdot \max\left(\frac{1}{(SF_{LP} \cdot s_1'(t))}\frac{1}{b_p}\frac{dE_{total}}{d\ SFW}.\frac{d\ SFW}{dt}\right) \tag{20}$$

Then, the substitution of Eq. (19) into Eq. (20) results in,

$$CRSS_{MCS} = SF_F \cdot \max\left(\frac{1}{(SF_{LP})}\frac{1}{b_p}\frac{dE_{total}}{d\ SFW}\right) \tag{21}$$

Therefore, the CRSS is rewritten as follows,

$$CRSS_{MCS} = \frac{SF_F}{b_p \cdot SF_{LP}} \cdot \max\left(\frac{dE_{total}}{dSFW}\right) \tag{22}$$

For the solution B of isolated motion, Eq. (19) is repeated for all segments (along either s_1 or s_2 axis), which also yields Eq. (22) from Eq. (16). The maximum derivative occurs at the convergence limit by using the partial dissociation for $\gamma_{cisf} < \gamma_{isf} \leq 0$. The CRSS of the zero γ_{isf} case, for instance, is determined as 290 MPa with the given material constants. Based on the framework described, we study stability, SFW, and CRSS maps with various material constants in Section 3.

3. Results and discussion

3.1. Stability of partial dissociation

The characteristics of the negative γ_{isf} in current MCS framework are defined in the stable dissociation regime. It is important to note that the specific combination of material variables to guarantee stability will depend on the given material constants. The non-zero solutions such as SFW and CRSS therefore require the determination of γ_{cisf} baseline in the given material constants such as a, and elastic moduli of C_{11}, C_{12}, and C_{44} by modulating both γ_{us} and γ_{isf}. In Fig. 6, we calculate the stability regimes for each material parameter and correlate both γ_{us} and γ_{isf} in the domain, which are novel findings in the first place. Fig. 6 indicates stable and unstable regimes by varying lattice constant (a) within 3.6–5.6 Å. The other constants $\mu = (C_{11}\text{-}C_{12})/2$ and C_{44} are fixed as 34.5 GPa and 165 GPa. In the positive region of γ_{isf}, the stability condition of $\gamma_{us} > \gamma_{isf}$ is set to be always satisfied, which is already known in the conventional theory. In the negative region of γ_{isf}, as explained in Section 2.3, the determination of the initial zero derivative of E_{total} is numerically implemented on each point of SFEs (γ_{us}, γ_{isf}) based on the given material constants. In a slightly negative γ_{isf}, the dissociation stress hypothetically requires a high level of γ_{us} to make the materials stable. Then, in a highly negative region, the increase falls short of ensuring stability. Any SFE (γ_{us}, γ_{isf}) points outside the envelopes are considered unstable ones that rarely follow FCC dislocation motion. As a increases, the baselines of stability move upward in the SFE (γ_{us}, γ_{isf}) domain.

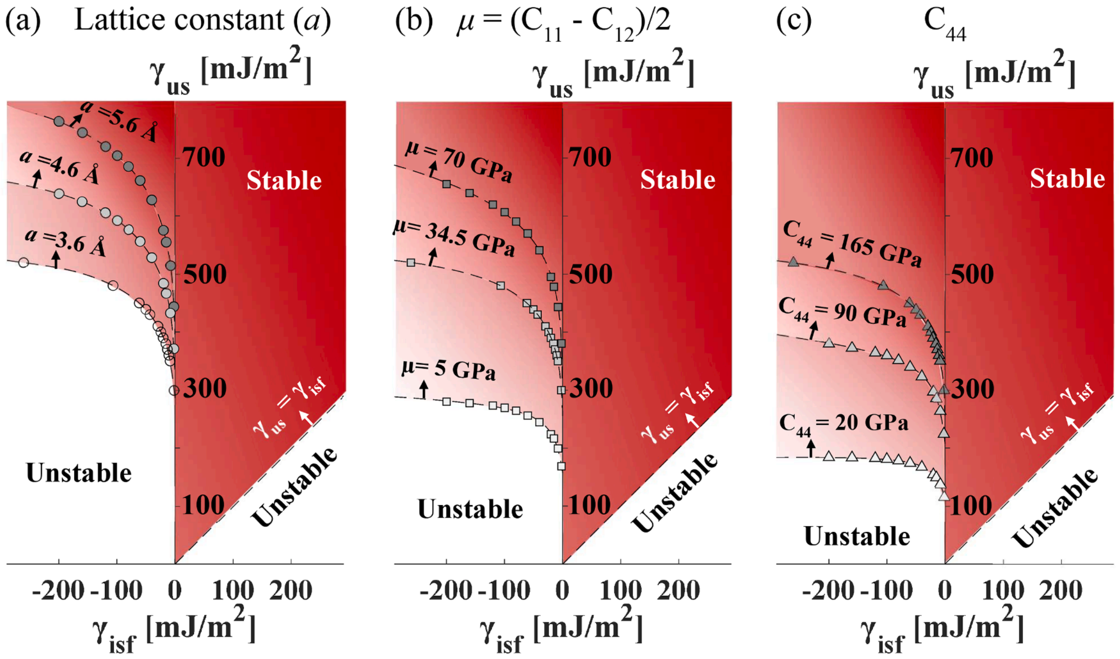

Fig. 6. Stable and unstable regimes (a) varying lattice constant (a), and elastic moduli of (b) $\mu = (C_{11} - C_{12})/2$, and (c) C_{44}; All critical negative γ_{cisf} points (baselines) are numerically determined at each unstable stacking fault energy (γ_{us}) by using the given material constants a, C_{44}, and μ. The initial envelope has $a = 3.6$ Å, $\mu = 34.5$ GPa, and $C_{44} = 165$ GPa, and each material constant is respectively varied (arrow) to determine the stable envelope of SFEs. In the positive region of γ_{isf}, the stability condition of $\gamma_{\mathrm{us}} > \gamma_{\mathrm{isf}}$ is set to be always satisfied. Any regimes that are out of the envelopes are considered unstable dissociations which rarely follow FCC dislocation motion. Stable regimes are gradually colored as a red shading for each material constant, where the most stable regime is colored as the strongest red.

In Fig. 6b and c, the determination of stable regimes is similarly implemented for each effect on elastic moduli. We investigate the envelopes for $\mu = (C_{11} - C_{12})/2$ and C_{44}, and the lattice constant is fixed as $a = 3.6$ Å. As μ and C_{44} decrease, the baselines of stability also move upward in (γ_{us}, γ_{isf}) domain. Therefore, all three material constants (a, μ, and C_{44}) contribute to the stability of FCC dissociation. The distinctive correlations between those constants and the CRSS have been also verified in the previous work (You et al., 2023). Similarly, the dependencies of a, μ, and C_{44} on the stabilities can be deduced by the equilibrium core-widths (ξ^0_{LP}, ξ^0_{TP}), as determined in Eq. (18). The decreases in the elastic moduli μ and C_{44} consequently result in narrower cores in each partial dislocation, which are mediated by the strain-energy E_{strain} between two partials and the WS cell-based misfit energy E_{misfit} in the FCC lattice slip plane. As the material constants (a, μ, and C_{44}) are reduced, the E_{strain} is lowered in the interaction of two partials, and for a given E_{misfit} the dislocation cores become narrower. The stability of materials with respect to a is also similarly related to ξ^0_{LP} and ξ^0_{TP}, based on the contribution of lattice spacing in E_{misfit}. The findings in this work suggest the correlations between material constants, stabilities, SFW, and the CRSS. In the following results, the SFW and CRSS are also described, and the characteristics are similarly mediated by the effect of narrower ξ^0_{LP} and ξ^0_{TP}.

3.2. Finite stacking fault width

Fig. 7 demonstrates the SFW contours upon stable regimes of both SFEs (γ_{us}, γ_{isf}) domains. In Fig. 7a, we plot the global equilibrium SFW (SFW₀) as only determined in the positive γ_{isf} using Eq. (10). As the SFEs (γ_{us}, γ_{isf}) approach closer to the conventional stability condition ($\gamma_{\mathrm{us}} \approx \gamma_{\mathrm{isf}}$), SFW₀ results in no solution (closely zero SFW). As the positive γ_{isf} decreases and approaches zero, then SFW₀ diverges as infinity. This is also consistent with the classical formula, as stated in Eq. (1). γ_{us} can also contribute to the SFW₀ at the overall domain, while γ_{isf} becomes dominant at a higher level of γ_{us}. Fig. 7b depicts the SFW for the first local minimum ($\mathrm{SFW_{min}}$) of E_{total}. Similarly, $\mathrm{SFW_{min}}$ is bounded by the stability conditions of $\gamma_{\mathrm{us}} > \gamma_{\mathrm{isf}}$ as well as $\gamma_{\mathrm{us}} > \gamma_{\mathrm{cisf}}$. The baseline γ_{cisf} is determined in Fig. 6 based on material constants are $a = 3.6$ Å, $\mu = 34.5$ GPa, and $C_{44} = 165$ GPa, respectively. The $\mathrm{SFW_{min}}$ also yields no solution as SFEs (γ_{us}, γ_{isf}) approach to the conventional stability condition ($\gamma_{\mathrm{us}} \approx \gamma_{\mathrm{isf}}$). However, both SFEs ($\gamma_{\mathrm{us}}$, γ_{isf}) are critical to determining the $\mathrm{SFW_{min}}$ at the overall domain, which is not fundamentally established before. Then, the $\mathrm{SFW_{min}}$ keeps increasing toward infinity as the SFEs (γ_{us}, γ_{isf}) approach the new stability condition baseline with the γ_{cisf}.

From both contours of SFW₀ and $\mathrm{SFW_{min}}$ in Fig. 7, any FCC materials can be investigated for finite SFWs. Based on the stability regime, one may identify how much the level of SFEs (γ_{us}, γ_{isf}) is required to get finite SFW at both positive and negative γ_{isf} sides. For the positive γ_{isf}, there is the maximum limit converged for the SFW (Fig. 7a), although the least possible SFW can be characterized as well (Fig. 7b). This can be applied as a variation of SFW in the practical experiments. For the negative γ_{isf}, the non-zero solutions of

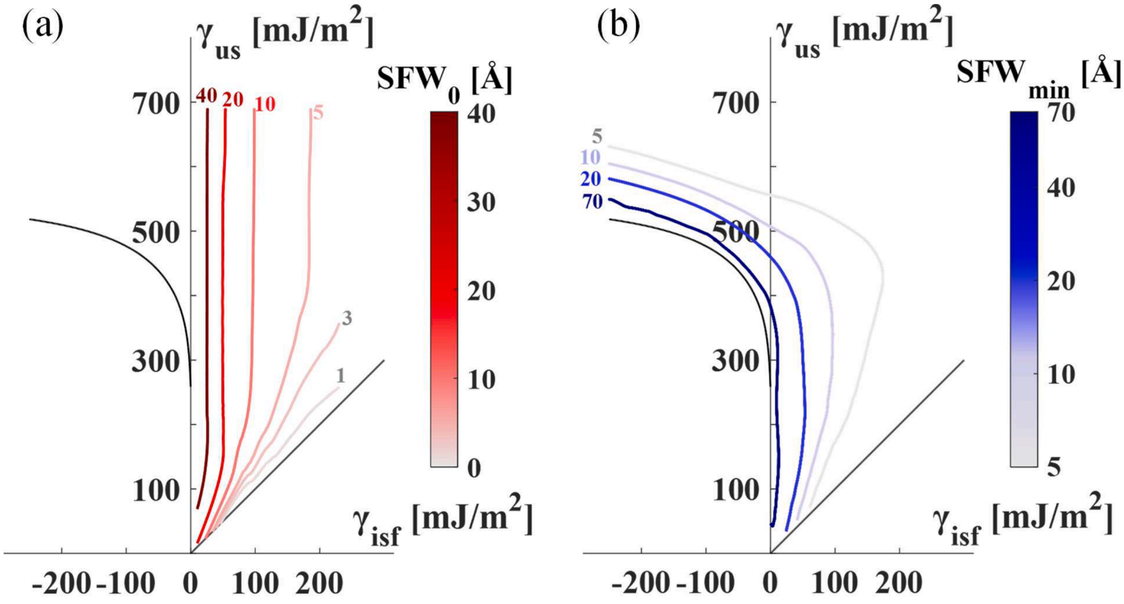

Fig. 7. Stacking fault width (SFW) contours upon stable regimes of stacking fault energies (γ_{us}, γ_{isf}): (a) the SFW for the global minimum (SFW_0) of total energy, and (b) the SFW for the first local minimum (SFW_{min}) of total energy; SFW_0 is bounded by $\gamma_{isf} > 0$ and $\gamma_{us} > \gamma_{isf}$ since it goes to infinite or is not defined at $\gamma_{isf} \leq 0$ and $\gamma_{us} \leq \gamma_{isf}$. Similarly, SFW_{min} is bounded by two stability conditions of $\gamma_{us} > \gamma_{cisf}$ and $\gamma_{us} > \gamma_{isf}$ on the negative and positive sides of γ_{isf}, respectively. Material constants are a = 3.6 Å, μ = 34.5 GPa, and C_{44} = 165 GPa.

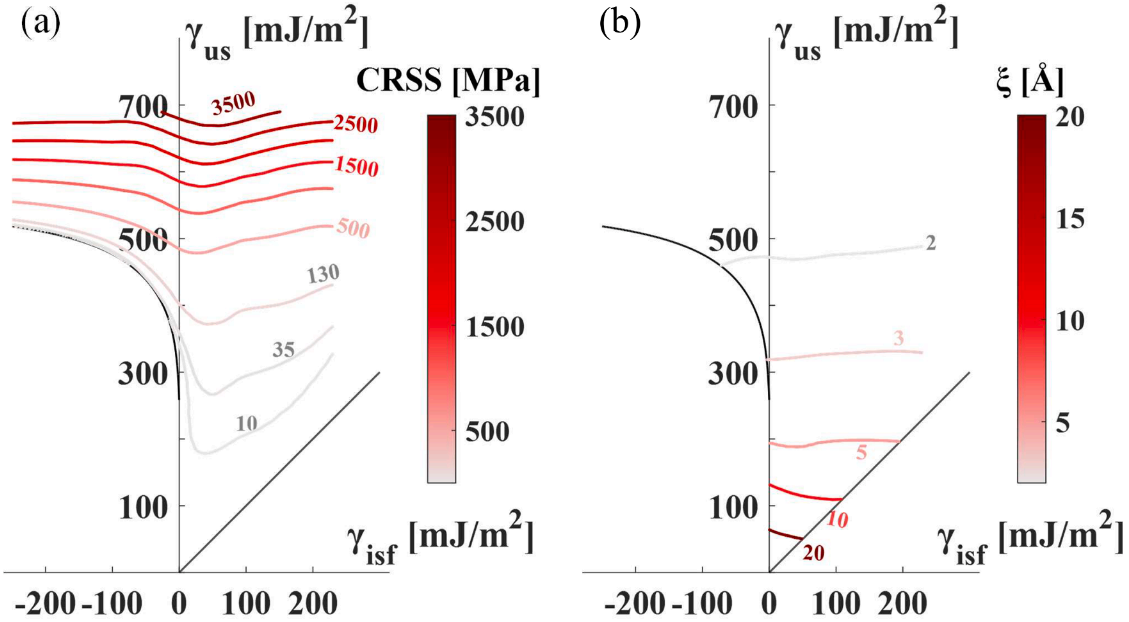

Fig. 8. Contours upon stable regimes of stacking fault energies (γ_{us}, γ_{isf}): (a) Critical resolved shear stress (CRSS), and (b) core-widths (ξ); CRSS is bounded by two stability conditions of $\gamma_{us} > \gamma_{cisf}$ and $\gamma_{us} > \gamma_{isf}$ on the negative and positive sides of γ_{isf}, respectively, as it becomes undefined outward the stable curves. Material constants are a = 3.6 Å, μ = 34.5 GPa, and C_{44} = 165 GPa, respectively.

SFW are available in the stability regime. The SFW for the negative γ_{isf} can also diverge at the new criterion of baseline. Therefore, materials with negative γ_{isf} may result in a large variation of SFW. We note that, however, all the other material constants (a, μ, C_{44}, and γ_{us}) should be precisely measured since they are critically paired with the determination stability and SFWs. Along the contour with the same level of SFW_{min}, there are multiple solutions for SFEs (γ_{us}, γ_{isf}), so theoretical studies on SFEs are independently recommended. All the SFEs outside the stability hypothetically imply that no FCC materials can stand with respect to the dissociation of Shockley partials. Therefore, if three material constants (a, μ, and C_{44}) are only known without prior experimental knowledge, one can theoretically deduce which level of SFEs yields finite SFW with stable dissociation or other phases with different dissociation in unstable regimes.

3.3. CRSS and core-widths

Fig. 8 represents the CRSS and core-widths computed along the MEP on the E_{total} landscape in this study. In Fig. 8a, the CRSS contours include the results based on both Eqs. (16) and (22). Along the stability conditions of both $\gamma_{\mathrm{us}} > \gamma_{\mathrm{cisf}}$ and $\gamma_{\mathrm{us}} > \gamma_{\mathrm{isf}}$, the CRSS approaches zero. It also yields no solution outside the conditions, which is negative dissociation stress. The CRSS exponentially increases as γ_{us} rises, which is also known for the positive side of γ_{isf} in the previous study (You et al., 2023). The elevation of γ_{isf} is also distinctive to characterize the CRSS, although it has a fluctuating trend. This usually stems from the discretization of misfit energy along the MEP. For the WS cell-based E_{misfit} in Eq. (9), the number of WS cell area is divided as cumulative summation within integers. Also, E_{misfit} variation along the MEP has distinctive WS cells to calculate the resolved path and slope of E_{total}. Therefore, the intrinsic stacking fault point coming from the disregistry domain also reflects discontinuous variation followed by its correlation with the CRSS, which is different from the SFW trend.

In Fig. 8b, we plot equilibrium core-widths of partial dislocations (ξ^0_{LP}, ξ^0_{TP}), as both denoted as (ξ) for a screw dislocation. It includes the results from both minimization Eqs. (10) and (18). The equilibrium core-widths (ξ) on the negative side of γ_{isf} in this material constants ($a = 3.6$ Å, $\mu = 34.5$ GPa, and $C_{44} = 165$ GPa) are usually less than 3 Å. We have narrower symmetric cores for the negative γ_{isf} in each partial dislocation. As we demonstrate the correlation of material constants and core-widths, they are mediated by the strain-energy E_{strain} between two partials and the WS cell-based misfit energy E_{misfit} in the FCC lattice slip plane. The narrowly concentrated dislocation cores, therefore, result in possibly higher CRSS. This is also validated with the positive γ_{isf} materials in the previous study (You et al., 2023). As the SFEs (γ_{us}, γ_{isf}) approach the origin, the equilibrium core-widths (ξ) diverge and yield the zero CRSS where infinite SFWs are found in both SFW_0 and $\mathrm{SFW}_{\mathrm{min}}$.

3.4. Comparison of results with experimental data

We demonstrate the MCS framework in extended region of the SFEs (γ_{us}, γ_{isf}) to illustrate stability, finite SFW, and CRSS. Here, we further benchmark how the formalism works well with well-known material with a negative γ_{isf}. Most of the MHEAs have been shown to possibly have negative γ_{isf}. Still, some of them are reported to have finite SFW in experiments. Therefore, one of the MHEAs can be an excellent candidate to validate the formalism in this work. Nevertheless, not all material constants are compatibly available within the consistencies in MD or experiments. Hence, we choose NiCoCr MEA, demonstrated in Section 2.3 and Fig. 4. NiCoCr MEA is the one, to the best of our knowledge, that shows the most consensus to have a negative γ_{isf} in the previous studies (Alkan et al., 2018a; Celebi et al., 2022; Chandran and Sondhi, 2011; Datta et al., 2009; Ding et al., 2018; Huang et al., 2018; LaRosa and Ghazisaeidi, 2022; Li et al., 2022; Niu et al., 2018; Shang et al., 2012; Siegel, 2005; Sun et al., 2021; Tian et al., 2017; Wang et al., 2018a; Zhang and Wang, 2022; Zhang et al., 2017a, 2017b; Zhao et al., 2019, 2017). Other MHEAs can have varying γ_{isf} on both positive and negative sides, but some benchmarks are made in Table B1 in the Appendix B. We choose $\gamma_{\mathrm{isf}} = -10$ mJ/m^2 for NiCoCr case, demonstrated in Section 2.3 ($\gamma_{\mathrm{us}} = 418$ mJ/m^2) and Fig. 4, which is a slightly negative value among the independent theoretical results of γ_{isf}. In Appendix B, other hypothetical combinations of (γ_{us}, γ_{isf}) for NiCoCr are demonstrated in Fig. B1. We tabulate the reported γ_{isf} of equiatomic MHEAs available in **Table S1** in Supplementary Material. By carefully choosing other material constants ($a = 3.559$ Å (Huang et al., 2018), $\mu = (C_{11} - C_{12})/2 = 45.2$ GPa, $C_{44} = 138.4$ GPa (Laplanche et al., 2020)), the stability, SFW, and CRSS can be achieved. If the moduli and lattice constants differ (i.e., lower values), it is possible that γ_{isf} value lower than -10 mJ/m^2 could give a finite SFW as well. The critical curves point to strong sensitivity to moduli and lattice constants. We utilized the values for the single crystal constants obtained from the literature experiment as described in the paper. For the screw case, we systematically demonstrate the procedure for determining the SFW in Section 2.3 and Fig. 4.

Regarding the SFW we offer the following discussion. The classical relationship, Eq. (1) has been used with a positive SFW to infer γ_{isf}, usually in the range of +10 to +20 mJ/m^2. However, by using the negative value of γ_{isf} in this work, the theory predicts the finite experimental SFW without recourse to Eq. (1). The current study accounts well for all the phenomena mentioned earlier involved in the motion of the extended dislocation of non-positive γ_{isf} in FCC materials. We also acknowledge that other factors influence the SFWs such as short-range ordering (SRO), atomic-level compositional variations, i.e., solute effects, and non-straight dislocation lines (with local curvature). These aspects might have an impact on compositionally complex alloys. The current study corrects the computation of the classical SFEs (γ_{us}, γ_{isf}) and SFW by including a first-order effect that has not been considered in previous publications. Future studies will need to focus on further improvements to account for other factors as well.

Then, we further calculate the properties, including the CRSS in different dislocation characters such as $\theta = 60^\circ$ In the range of experimental results, the $\mathrm{SFW}_{\mathrm{min}}$ and CRSS agree well with the MCS formalism, as shown in Table 1. The predictions for pure screw and 60° are similar (148 MPa) and agree with experiments at 77 K (140–160 MPa) that pinpoint precisely the onset of slip. There have been debates on the role of solid solution hardening (SSH) versus SRO in NiCoCr. Suffice it to say that these other effects are manifested through the fault energies associated with multi-elements on the slip plane (WS lattice). The SSH contribution calculations in the literature for the edge dislocation case result in 124.1 MPa at low temperatures (see Appendix D), which is below the experimentally reported results. It is our intention to address these calculations in later studies.

Table 1

A summary of results for NiCoCr medium entropy alloy. For the cases of experimental SFWs and CRSS, the ranges are shown. For the negative γ_{isf}, a slightly low value of -10 mJ/m^2 is chosen in the simulations. The framework in this work is in excellent conversion to the experiments based on the negative γ_{isf}, particularly considering the dislocation character effects (screw and 60° cases). The experimental SFWs and CRSS are from elsewhere (Abuzaid and Patriarca, 2020; Laplanche et al., 2017; Liu et al., 2018; Shih et al., 2021).

Material	γ_{isf}	SFW (Expt.)	SFW$_{min}$ (this study)	CRSS (Expt.)	CRSS (this study)
NiCoCr	-10 mJ/m^2	3.96 ~ 7.25 nm (screw, $\theta <$ ~3°) 7.72 ~ 14.92 nm ($\theta =$ ~60°)	5.55 nm (pure screw, $\theta = 0°$) 10.76 nm ($\theta = 60°$)	140 ~ 160 MPa (Single crystal at 77 K)	148.3 MPa (pure screw, $\theta = 0°$) 148.5 MPa ($\theta = 60°$)

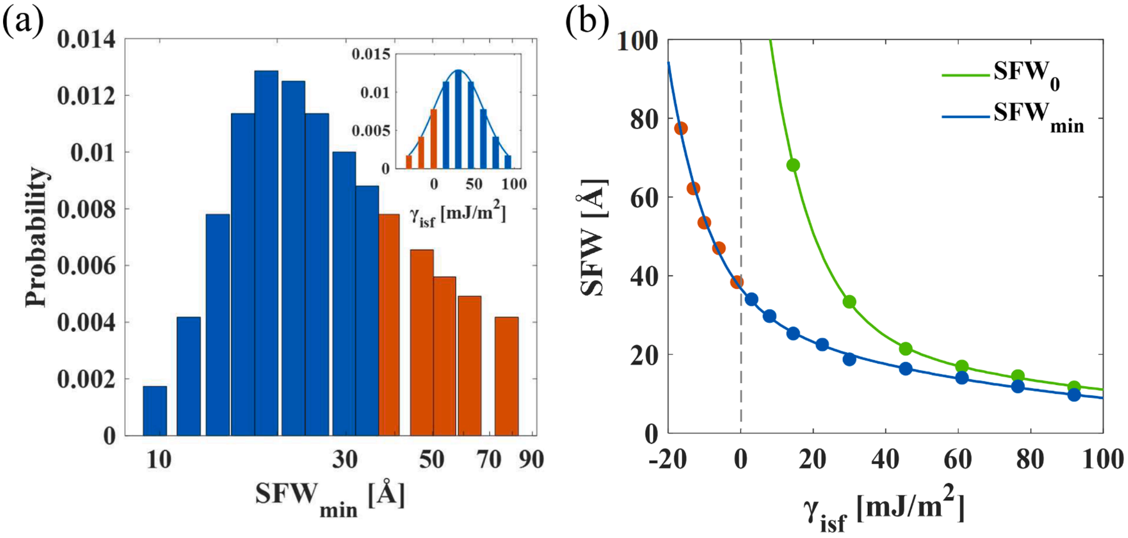

Fig. 9. (a) Probability of SFW$_{min}$ distribution based on its γ_{isf} (inset), and (b) two functionals of SFW$_0$ and SFW$_{min}$ for the MCS framework with respect to γ_{isf}. Datapoints in the positive and negative γ_{isf} region are colored blue and orange in both figures.

3.4. *Distribution of stacking fault energy*

Experimental findings point to various stacking fault widths in NiCoCr alloys. A similar distribution of the SFE in the microstructure is expected due to local variations in chemistry and the positioning of atoms along the slipped region. Therefore, we can demonstrate an extended MCS framework for hypothetical variations in SFEs in NiCoCr, based on the reported values (mean 30 mJ/m^2, and standard deviation 31 mJ/m^2) (Ding et al., 2018). In Fig. 9a, the normal distribution of probability in γ_{isf} is depicted as an inset, and the calculated SFW$_{min}$ values based on the sampled γ_{isf} are represented. The sampled region of γ_{isf} distribution covers -32 mJ/m^2 ~ 92 mJ/m^{2,} while the unstable dissociation stress is found at $\gamma_{isf} < -16.5$ mJ/m^2. In the stable negative γ_{isf} region, the SFW$_{min}$ extends from 38.4 Å to 77.4 Å corresponding to -1 mJ/m^2 to -16.5 mJ/m^2. Therefore, as γ_{isf} approaches its critical point, the probability of SFW$_{min}$ remains a narrow fraction of the skewed distribution, since the SFW$_{min}$ exponentially increases. This is unlike the normal distribution of the γ_{isf}. In Fig. 9b, the exponential increases of two functionals of SFW$_0$ and SFW$_{min}$ are depicted with respect to γ_{isf}. The hypothetical probability is symmetric on the mean γ_{isf} ~ 30 mJ/m^2 (SFW$_{min}$ ~ 18.8 Å, SFW$_0$ ~ 33.4 Å), so possibly γ_{isf} ~ -16.5 mJ/m^2 (SFW$_{min}$ ~ 77.4 Å) and γ_{isf} ~ 76.5 mJ/m^2 (SFW$_{min}$ ~ 11.9 Å) have the same probabilities. The skewed SFW distribution shape can also be found in experimental observations in water-quenched NiCoCr (Zhang et al., 2020), compared to the aged sample showing the normal distribution and lower SFW (possibly higher γ_{isf}). Thus, the results provide further insight into the role of a possible γ_{isf} distribution in generating a skewed SFW distribution.

3.5. *Character effect in stable/unstable operational regimes*

As shown in Fig. 2, the character effect is denoted by the angle θ. For general hypothetical materials with negative γ_{isf}, the dislocation character effect can be further investigated. In the main results above (Figs. 3–9), we demonstrated that for the pure screw character case, and the intermittent motion of partial dislocations is energetically equivalent to the isolated motion with fixed one partial. We here apply the isolated motion for varying dislocation characters from the pure screw ($\theta = 0°$) to the pure edge ($\theta = 90°$). In Fig. 10, the maximum dissociation stresses at the convergence are shown for slightly negative γ_{isf} material (-5 mJ/m^2) based on two different scenarios: i) LP is moving, and TP is fixed, or ii) vice versa. γ_{us} is selected as the maximum hypothetical limit of 740 mJ/m^2, and the elastic constants are taken from NiCoCr ones ($a = 3.559$ Å (Huang et al., 2018), $\mu = 45.2$ GPa, $C_{44} = 138.4$ GPa (Laplanche et al., 2020)). Pure screw, 30°, 60°, and pure edge characters only represent the stable (positive) dissociation of dislocation, while other

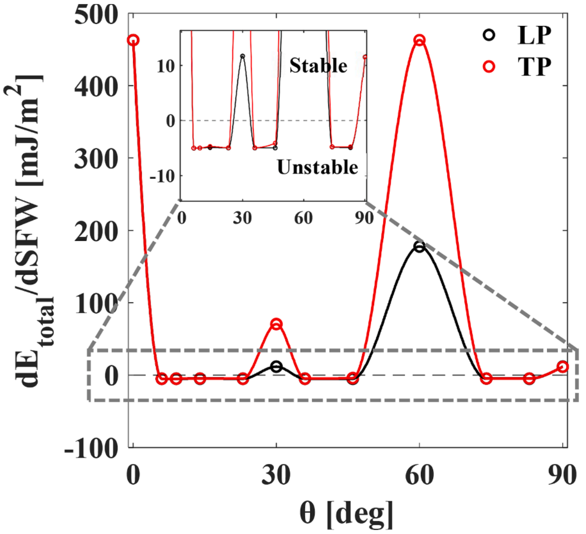

Fig. 10. Dissociation stresses upon varying dislocation characters from pure screw ($\theta = 0^\circ$) to the pure edge ($\theta = 90^\circ$). For the validation of stability, the maximum dissociation stress at the convergence state (SFW $> 2 \times 10^4$ Å) is taken. Dislocation characters with unstable dissociation are enlarged in the inset figure. Each black or red datapoint represents which partial dislocation is respectively moving.

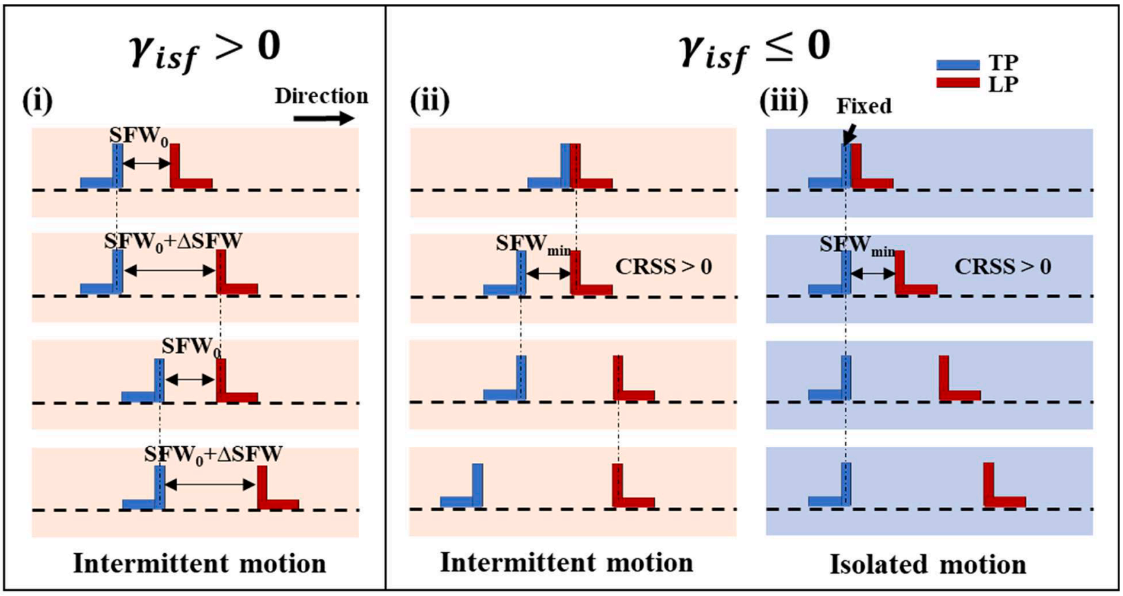

Fig. 11. Different scenarios of dislocation motion concerning γ_{isf} and dislocation character (TP=trailing partial, LP=leading partial). (i) Energetically favorable intermittent motion for $\gamma_{isf} > 0$. The red moves- blue is fixed (second row), followed by blue moves- red is fixed (third row), then red moves- blue is fixed (fourth row). Such motion produces flow at lower CRSS. For mixed dislocation characters, the CRSS is direction-dependent (motion to the right versus left) (ii) Intermittent motion for $\gamma_{isf} \leq 0$-for all characters; two different directions (forward versus reverse) are energetically the same. (iii) Isolated motion where one partial is fixed (TP in this case) and the other is freely moving for $\gamma_{isf} \leq 0$. For pure screw ($\theta = 0^\circ$) and edge (90°) characters, both cases for which LP or TP is fixed are energetically the same as the intermittent motion. However, for mixed characters, the intermittent ((i) and (ii)) and the isolated motions (iii) with LP or TP moving have all different energetics.

minor characters are unstable (negative stress), as shown in the inset figure. This implies that γ_{cisf} will increase on most of dislocation characters, compared to pure screw, as the dissociation stress decreases except 60° mixed dislocation. Either screw and 60° case can be the maximum peak for a given material, which agrees well with the CRSS variation from the previous works (Celebi et al., 2023). In two different isolated motions, pure screw and pure edge characters have a symmetricity, i.e., irrespective of whether one partial is moving or fixed, the result remains the same.

On the other hand, the other characters present asymmetry (Fig. 10). This asymmetry becomes substantial for 30° and 60° characters,

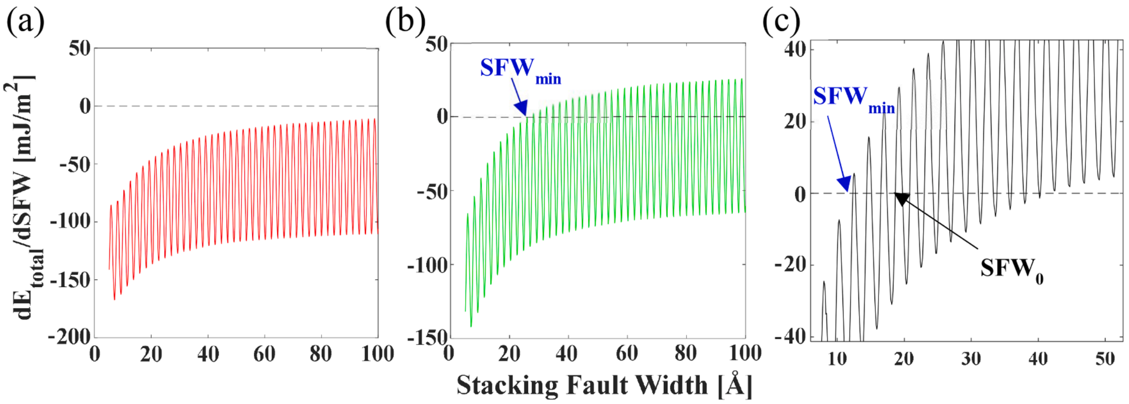

Fig. A1. Derivatives of total energy E_{total} at low SFW region. (a) $\gamma_{isf} = -50$ mJ/m^2, (b) $\gamma_{isf} = 0$ mJ/m^2, and (c) $\gamma_{isf} = +50$ mJ/m^2. Material constants are a = 3.6 Å, μ = 34.5 GPa, C_{44} = 165 GPa, γ_{us} = 439 mJ/m^2. The minimum threshold of SFW is SFW > $2\xi_P$.

Table B1
Benchmarks of the extended MCS framework on different alloys. Among input material constants, γ_{us} and γ_{isf} are hypothetically changed since these materials have inconsistencies in the reported γ_{isf}.

Materials	a [Å]	C_{11} [GPa]	C_{12} [GPa]	C_{44} [GPa]	γ_{us} [mJ/m^2]	γ_{isf} [mJ/m^2]	CRSS$_{MCS}$ [MPa]	CRSS$_{Expt.}$ [MPa]
$Ni_{33.3}Co_{66.7}$	3.52	238.7	155.3	131.5	205	+20	4.2, 13.8*	~15[a]
					205	0	~ 0	(RT)
NiCoCrFe	3.53	219	126	130	303	−11	Unstable	~99[b]
					374	+10	125	(77 K)
					374	0	121.7	
					360	0	92.7	
					364	0	99.1	
					374	−5	87.0	
NiCoCrFeMn	3.60	221	152	165	281	−7	Unstable	~172[c]
					281	0	9.2	(77 K)
					380	−31	Unstable	
					380	0	111.8	
					400	0	159.5	
					439	+8	177	

* 60° mixed dislocation.
[a] Ref. (Chowdhury et al., 2015).
[b] Ref. (Wu et al., 2015).
[c] Ref. (Abuzaid and Sehitoglu, 2017).

representing the higher dissociation stress for TP when LP is fixed. Therefore, the dissociation of partials is relatively stable and favorable in the direction of TP motion. We elaborate on this finding in the next section.

3.6. Intermittent versus isolated motion of partials

The solution for slip motion exhibits asymmetry for mixed dislocation characters, i.e., the CRSS corresponding to LP and TP motions differ. This behavior is not only confined to the negative γ_{isf} but can occur in positive γ_{isf} regimes, but the details differ, as we explain below. We describe all possible scenarios in Fig. 11 for the two γ_{isf} regimes. We first discuss the $\gamma_{isf} > 0$ cases. For materials with $\gamma_{isf} > 0$, (i) the intermittent motion in either direction is energetically preferable where one of the partials moves first, followed by the other partial. This scenario holds since there is a positive contribution by misfit energy for increasing the SFW as discussed in Fig. 1. In Fig. 11 for $\gamma_{isf} > 0$ in the mixed dislocation case (i), two different directions (e.g., right or left in the figure) are not equivalent, preferring one over the other.

However, for $\gamma_{isf} \leq 0$, there are two possible scenarios: (ii) the partials can still dissociate intermittently, or (iii) TP can be fixed in position when LP is freely moving, or vice versa. Since no energy component increases for the $\gamma_{isf} \leq 0$ cases, the global equilibrium is at infinity, and the local equilibrium exists at a finite dissociation.

Nevertheless, for pure screw and edge dislocation characters, at $\gamma_{isf} \leq 0$, (ii) intermittent motions are energetically the same as (iii) isolated motion(s). For mixed dislocation characters, however, their energetics differ. Therefore, for $\gamma_{isf} \leq 0$ in the mixed dislocation case, (ii) the intermittent motion is still energetically the same in forward vs. reverse motion directions. But, for the (iii) case of isolated motion, (last column) the energetics are different. The forward motion is shown as an example. This may have implications for tension-compression asymmetry in FCC materials, including the MHEAs.

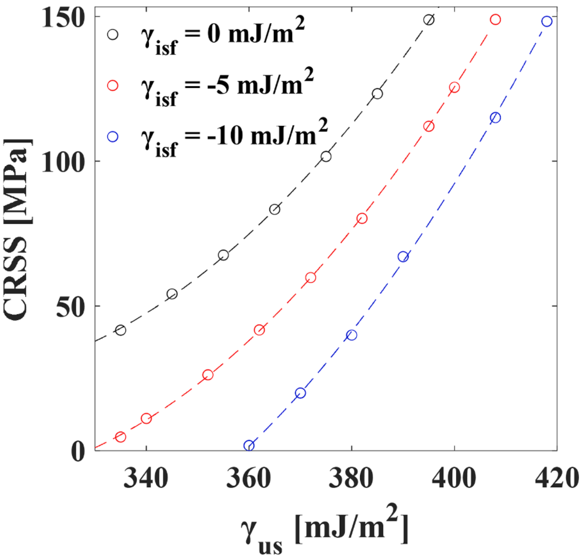

Fig. B1. CRSS contours upon hypothetically changing SFEs (γ_{us}, γ_{isf}) for NiCoCr based on the material constants a = 3.559 Å, μ = 45.2 GPa, and C_{44} = 138.4 GPa, respectively.

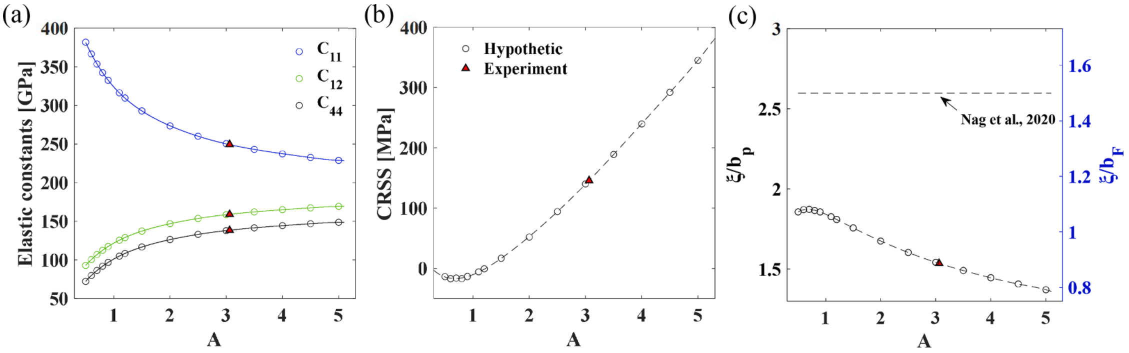

Fig. C1. Effect of elastic anisotropy in NiCoCr: (a) The hypothetical variation of the anisotropy ratio, A, for various values of the single crystal constants. All the constants produce the same μ^{V}_{avg} and ν^{V}_{avg} corresponding to NiCoCr. The specific single crystal constants (C_{11} = 249.4 GPa, C_{12} = 159 GPa, and C_{44} = 138.4 GPa) are marked with red triangles; (b) Simulations of CRSS corresponding to hypothetical values of the anisotropy ratio A. The value A = 3.02 corresponds to the specific NiCoCr alloy resulting in the CRSS of 148.3 MPa; (c) The assumption of dislocation core-width/burgers vector (ξ/b_F) as 1.5 in the literature is compared to the MCS model simulations (shown with data points). The A = 3.02 corresponds to NiCoCr and results in a ratio of 0.887. The consequence of this result is that the previous models will underpredict the lattice resistance.

4. Final comments

We draw attention to the determination of dislocation core-widths and SFW, the assumptions commonly made in the literature, and their implications. The widely stated assumptions have been the following: (1) The dislocation core-widths are assumed to be approximately $1.5b_F$ (Nag et al., 2020), (2) the SFW is assumed to exceed 6–$8b_F$ and the results are assumed insensitive to its value, (3) the elastic moduli are assumed to have a negligible effect on the results, and (4) one partial moves while the other is stationary, or both partials translate simultaneously in unison. These assumptions may hold in limited cases, but they will not generally lead to successful prediction of experimental results. For example, if the dislocation core-width is overpredicted, the strength attributed to other contributions is magnified, which could lead to incorrect interpretations. We address this point by changing the elastic anisotropy of NiCoCr case in Appendix C. While (2) is valid for equiatomic NiCoCr, (1) is not. For example, for the binary alloy, $Ni_{64}V_{36}$, where the γ_{isf} is close to the γ_{us}, (2) is not valid, while (1) may be approximately valid. For pure Al, (1) is approximately valid, but (2) is not valid (Celebi et al., 2023). While (4) is valid for NiCoCr, it is not for $Ni_{64}V_{36}$, Al, Ni, and many FCC metals.

We emphasize that we are describing a wide range of hypothetical compositions of FCC materials with intrinsic SFEs in the range of 750 to −200 mJ/m^2. In arriving at these energy values for specific alloy compositions, the standard procedure has been to utilize density functional theory (DFT) or molecular dynamics (MD). The DFT is preferred because reliable interatomic potentials for multi-element alloys are not available in MD. However, in the DFT calculations, substantial computational resources are needed when the

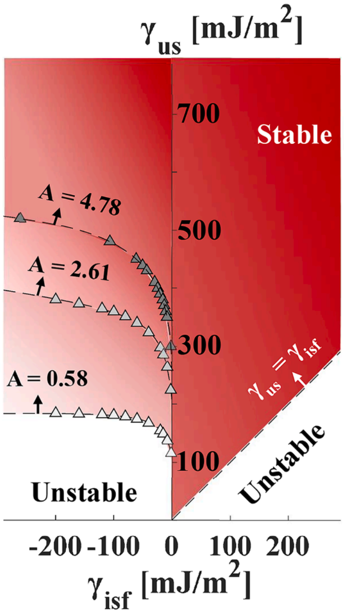

Fig. C2. Stable and unstable regimes varying the anisotropy ratio, A; The critical negative γ_{cisf} points are based on the data in Fig. 6c, by fixing lattice constant $a = 3.6$ Å, modulus $\mu = 34.5$ GPa. Any regimes that are out of the envelopes, including the conventional stability condition ($\gamma_{us} > \gamma_{isf}$), are considered unstable ones which rarely follow FCC dislocation motion. Stable regimes are gradually colored as a red scale for anisotropy ratio, A, where the most commonly stable is colored as the strongest red.

Table D1
A summary of the solid solution hardening (SSH) contribution in CRSS of edge dislocation in medium and high entropy alloys (MHEAs). Equiatomic ternary NiCoCr is one of multicomponent alloys that have negative SFEs in multiple independent studies. $CRSS_{SSH}$ for other alloys (NiCoCrFe, NiCoCrFeMn, $Ni_{33.3}Co_{66.7}$), suggested in Table B1 in Appendix B, are also tabulated here under the fixed core-width assumption $\xi / b_F = 1.5$.

CRSS	NiCoCr	NiCoCrFe	NiCoCrFeMn	$Ni_{33.3}Co_{66.7}$
$CRSS_{SSH}$ [MPa]	124.1*	85.5*	83.4*	5.2 (RT)
$CRSS_{Expt}$ [MPa]	~ 150 (77 K)	~ 99 (77 K)	~ 172 (77 K)	~ 15 (RT)

[*] Extracted from the previous works by (Varvenne et al., 2016; Yin et al., 2020).

number of atoms exceeds a few hundred. The following must be carefully noted: the placement of the atoms on the slip plane within the simulation box dictates the SFEs in alloys. To construct the atom distribution to mimic alloys, special attention must be devoted to obtaining energetically favorable configurations (Ding et al., 2018; van de Walle et al., 2013) with a finite number of atoms; then the slip cuts would result in the SFE that varies similar to real materials. The current simulations considered a distribution of SFEs in general conformity with experiments (Fig. 9).

The presence of SRO domains will also contribute to the local variations in the generalized energy levels (Zhang et al., 2020) and specifically the γ_{isf}. Such variations, including positive and negative SFEs, will produce a variation in SFWs (Chowdhury and Sehitoglu, 2017a; Laplanche et al., 2017). The model can predict the trends in the evolution of SFWs as the microstructure transitions to higher chemical SRO manifested through changes in energy levels. With an increase in SRO, the narrower SFW in experiments has been found in the 5 ~ 10 nm range, compared to 10 ~ 20 nm for smaller SRO cases in NiCoCr (Zhang et al., 2020). These trends are consistent with the findings in this work. If there are drastic changes in elastic constants due to compositional differences, the model will accommodate via the elastic strain-energy calculations. The role of elastic strain-energy E_{strain} has yet to be well understood. Still, it is clearly incorporated in the current model and can explain variations with a composition that is not evident based on the GSFE values alone. Further investigations are needed to explain all the trends observed experimentally.

We note the need to measure the CRSS in experiments precisely. Experiments on single crystals with digital image correlation resulted in a more precise level of 140–160 MPa (Abuzaid and Patriarca, 2020). If only polycrystalline data or RT is available, one must carefully evaluate the assumptions when correcting the polycrystalline data and thermal activation theory for temperature effects to obtain CRSS values. Also, regarding the temperature effect in the SFE, one may consider alternative methods such as ab-initio MD (de Koning et al., 1998; Wirth et al., 2022), and thermodynamic models (Curtze et al., 2011; Olson and Cohen, 1976; Togo and Tanaka, 2015). These studies noted that the SFE increases with increasing temperature for low γ_{isf} materials. In this study, we note that Figs. 6–8 cover a very wide range of SFE values, but we are not specifying the corresponding temperatures. This is outside the scope of our study.

Our approach's lattice resistance alone for screw and 60° cases agrees closely with the experimental results. The current results for strength elevation due to lattice resistance are sufficient to capture the experimental values. Therefore, the lattice resistance determination of negative SFE multi-component alloys, as proposed in this study, is a significant step toward advancing the understanding of mechanics of muti-component alloys. If the edge dislocation is considered, one would argue that the contributions from SRO or SSH are substantial. We investigate the SSH contribution in edge dislocation of MHEAs in Appendix D. In Appendix D, we show that the core-width assumption of $\xi/b_F = 1.5$ provides underestimation of experimental CRSS, depending on materials. In addition, we note that the SRO represents domains that undergo fault energy elevation upon slip, producing strengthening. The formulation for the SRO of negative SFE case and its change upon slip (Cohen and Fine, 1962) requires further studies and would provide further insights into CRSS contributions and will be considered in future work.

CRediT authorship contribution statement

Daegun You: Methodology, Investigation, Software, Formal analysis, Validation, Writing – original draft, Writing – review & editing, Visualization. **Orcun Koray Celebi:** Conceptualization, Methodology, Software, Investigation, Writing – original draft, Writing – review & editing, Supervision. **Ahmed Sameer Khan Mohammed:** Conceptualization, Methodology, Software, Investigation, Writing – original draft, Writing – review & editing, Supervision. **Huseyin Sehitoglu:** Conceptualization, Investigation, Supervision, Project administration, Funding acquisition, Writing – review & editing.

Declaration of Competing Interest

The authors declare that they have no known competing financial interests or personal relationships that could have appeared to influence the work reported in this paper.

Data availability

Data will be made available on request.

Acknowledgments

The work is supported by the National Science Foundation (NSF) under award number CMMI-21–25821, which is gratefully acknowledged. In addition, the use of the Illinois Campus Cluster, a computing resource that is operated by the Illinois Campus Cluster Program (ICCP) in conjunction with the National Center for Supercomputing Applications (NCSA) and which is supported by funds from the University of Illinois at Urbana-Champaign, is also gratefully acknowledged.

Supplementary materials

Supplementary material associated with this article can be found, in the online version, at doi:10.1016/j.ijplas.2023.103770.

Appendix A. Derivative of total energy and finite stacking fault width

For $\gamma_{\text{isf}} \leq 0$, the derivative of total energy E_{total}, including strain and misfit energies, is assessed as the dissociation stress of partials. The fluctuations that stem from Peierls valleys can intersect with zero dissociation stress, which results in the least finite SFW (SFW_{min}) for all regimes of γ_{isf}. In Fig. A1, the derivatives for three γ_{isf} cases are represented for $\gamma_{\text{isf}} = -50$ mJ/m^2, 0 mJ/m^2, and $+50$ mJ/m^2. For $\gamma_{\text{isf}} = -50$ mJ/m^2, the infinite SFW is required to intersect zero dissociation stress, while the finite SFWs are available for $\gamma_{\text{isf}} = 0$ mJ/m^2, and $+50$ mJ/m^2. Meanwhile, the global equilibrium (SFW₀) cannot be resolved for the $\gamma_{\text{isf}} = 0$ mJ/m^2 case since no misfit energy component attracts the lattice repulsed by the strain-energy. For $\gamma_{\text{isf}} = +50$ mJ/m^2, SFW₀ is found at the balance between the strain and misfit energies.

Appendix B. Hypothetical variation of SFEs in alloys and CRSS

Most reported MHEAs can theoretically have multiple γ_{isf} on both positive and negative sides, as tabulated in **Table S1** in Supplementary Material. Nevertheless, we select a few materials to benchmark the extended model by hypothetically changing γ_{us} and γ_{isf}. In Table B1, we tabulate input material constants (a, C_{11}, C_{12}, C_{44}, γ_{us}, and γ_{isf}) and the resultant CRSS of each case for three alloys ($Ni_{33.3}Co_{66.7}$, NiCoCrFe, and NiCoCrFeMn). The input constants can be found elsewhere in (Alkan et al., 2018a; Chowdhury et al., 2015; Huang et al., 2018; Niu et al., 2018, 2016; Zhang and Wang, 2022) or **Table S1** in Supplementary Materials. Among the reported equiatomic MHEAs, the NiCoCr case has the least inconsistency in theoretical SFEs and mostly shows $\gamma_{\text{isf}} \leq 0$ in **Table S1** in Supplementary Material. We also further modulate both γ_{us} and γ_{isf} for NiCoCr in Fig. B1. For any alloys, including NiCoCr, the possible SFEs (γ_{us}, γ_{isf}) can be resolved in the current model, which are in agreement well with the experiments (Abuzaid and Patriarca, 2020; Abuzaid and Sehitoglu, 2017; Chowdhury et al., 2015; Wu et al., 2015). Therefore, the careful determination on SFEs (γ_{us}, γ_{isf}) is necessary, although other input constants (a, C_{11}, C_{12}, and C_{44}) also sensitively vary the result.

Appendix C. Elastic anisotropy with negative stacking fault energy

We demonstrate the effect of elastic anisotropy (Zener) ratio, $A = \frac{2C_{44}}{C_{11}-C_{12}}$, for the case of equiatomic NiCoCr in Fig. C1a. The reference elastic constants are $C_{11} = 249.4$ GPa, $C_{12} = 159$ GPa, and $C_{44} = 138.4$ GPa (Laplanche et al., 2020), as $A = 3.02$, which is considered high. The other points on the curve are constructed upon keeping the Voigt shear modulus ($\mu_{avg}^{V} = \frac{C_{11}-C_{12}+3C_{44}}{5}$) and Poisson's ratio ($v_{avg}^{V} = \frac{3B-2\mu_{avg}^{V}}{2(3B+\mu_{avg}^{V})}$) constant for the same alloy. This choice was made to assess the role of A on the CRSS and the dislocation core-widths in the following steps.

The influence of anisotropy is frequently thought to have a less than 15% effect on the results. However, those models use the incorrect assumption that the core-width is independent of the elastic strain-energy. We make the following observations on the current model. The elastic anisotropy in this work (the MCS model) is known to affect the elastic strain-energy. Since the core-width is determined from the minimization of total energy (which includes both elastic strain and misfit energies), the elastic strain-energy calculation is critical to calculating the dislocation core-width. The elastic strain-energy varies with dislocation character producing different core-widths. Fig. C1b demonstrates our finding that CRSS significantly depends on the A ratio. In fact, for $A < 1$, the CRSS levels are unstable. For $A > 1$, the CRSS increases with A, and the value of $A = 3.02$ for NiCoCr corresponds to 148.3 MPa. These results are for the screw dislocation case.

To comprehend the simulation results of the MCS-based model, we demonstrate the role of the anisotropy on the core-width dimensions. There has been a tacit assumption that the core-width to burgers vector (full dislocation) ratio is approximately 1.5. This level is marked in Fig. C1c with a horizontal line, along with our simulations that show that the ratio is 0.887, which is far less than 1.5 for most values of the parameter A. However, it is vital to note that the partial dislocations and their corresponding burgers vector must be considered when analyzing low SFE materials. Compared to experiments, the CRSS prediction in this work is accurate as we do not use the $\xi/b_F = 1.5$ assumptions.

In Fig. C2, we also investigate the stability envelope for the anisotropy ratio, A, by fixing lattice constant $a = 3.6$ Å, modulus $\mu = 34.5$ GPa, and varying C_{44}, as it is similarly implemented for C_{44} in Fig. 6c. As A decreases, the baseline (γ_{cisf}) of stability moves downward in SFE (γ_{us}, γ_{isf}) domain. The anisotropy ratio can also be a parameter to classify the stability of FCC dissociation. Then, the narrower equilibrium core-widths (ξ_{LP}^{0}, ξ_{TP}^{0}) in each partial dislocation would consequently result from the decreases in anisotropy ratio. This is mediated by the strain-energy E_{strain} between two partials and the WS cell-based misfit energy E_{misfit} in the FCC lattice slip plane.

Appendix D. Solid solution hardening effect in edge dislocation

The origin of strengthening in MHEAs is an ongoing debate. The SSH-effect studies have several inherent assumptions regarding elastic anisotropy and the treatment of dislocation core-widths, and the models should be treated as semi-empirical. Consequently, it is important to understand its relative contribution in comparison with lattice resistance. We undertake such a comparison for four materials employing the treatment by Varvenne et al. (2016) and Yin et al. (2020) for edge dislocations based on original derivations from Labusch (1970).

The main equation given in the SSH theory is given below.

$$CRSS_{SSH} = A_{\tau}\left(\frac{\Gamma}{b_F^2}\right)^{-\frac{1}{3}}\left(\mu_{avg}^{V}\frac{1+v_{avg}^{V}}{1-v_{avg}^{V}}\right)^{\frac{4}{3}}\left(\frac{\sum c_n \Delta\overline{V}_n^2}{b_F^6}\right)^{\frac{2}{3}} \tag{D1}$$

where $\Gamma = \alpha\mu_{110/111}b_F^2$ is line tension energy, $\alpha = 0.125$ is line tension parameter, $\mu_{110/111} = \frac{C_{11}-C_{12}+C_{44}}{3}$ is shear modulus in $\{111\}$ plane in $\langle 110\rangle$ direction, c_n is composition of constituent elements, and $\Delta\overline{V}_n$ is misfit volume parameter. The Voigt average of shear moduli μ_{avg}^{V} and Poisson's ratio v_{avg}^{V}, pre-factor A_{τ} (which depends on the anisotropy), the dislocation core-width, and finally the SFW, are also reflected in this equation. The following equation is utilized for volume misfit,

$$\Delta\overline{V}_n = \frac{\partial V_{alloy}}{\partial c_n} - \sum_{m=1}^{N} c_m \frac{\partial V_{alloy}}{\partial c_m} \tag{D2}$$

where $V_{alloy} = V_{alloy}(c_1, c_2, \ldots, c_{N-1})$ and $\frac{\partial V_{alloy}}{\partial c_N} = 0$ where compositions are known for a given alloy and the change in volume with concentration are calculated from atomistic methods. The assumed dislocation core-width, $\xi/b_F = 1.5$ is taken as a universal parameter for FCC metals and leads to $A_{\tau} = 0.01785$. We showed in Appendix C that the $\xi/b_F = 1.5$ assumption is inaccurate for NiCoCr. Neverthless, our aim is to establish SSH values in conformity with previous treatments and compare the results with the lattice resistance. So, for the purposes of consistentcy with previous SSH work (Yin et al., 2020), the same input parameters were used for NiCoCr ($C_{11} = 252$ GPa, $C_{12} = 158$ GPa, and $C_{44} = 142$ GPa), and the misfit parameters were taken as follows ($\Delta\overline{V}_{Ni} = -0.493$ Å^3, $\Delta\overline{V}_{Co} = -0.497$ Å^3, and $\Delta\overline{V}_{Cr} = +0.990$ Å^3). Then, the SSH contribution, i.e., $CRSS_{SSH}$ at 0 K, is obtained as 124.1 MPa using Eq. (D1). This prediction is below the average experimental level of 150 MPa at low temperatures (Abuzaid and Patriarca, 2020) and below the lattice resistance predictions in this work.

We also evaluate $CRSS_{SSH}$ for the NiCoCrFe and NiCoCrFeMn alloys (Varvenne et al., 2016). The results are shown with asterisks in

Table D1 and the SSH model underestimates the experimentally measured CRSS levels in all cases.

For the $Ni_{33.3}Co_{66.7}$ binary alloy, there were no $CRSS_{SSH}$ estimates to the best of our knowledge. So, we derive the misfit parameters based on the lattice constants for binary Ni-Co system from elsewhere (Nishizawa and Ishida, 1983), which gives $V_{alloy} = 11.13 - 0.1841c_{Ni}$, $\Delta\overline{V}_{Ni} = -0.123$, and $\Delta\overline{V}_{Co} = +0.307$. The experimental results $Ni_{33.3}Co_{66.7}$ are only available at room temperature. The thermal activation correction based on the equation below has been widely used,

$$CRSS_{SSH}(T,\dot{\varepsilon}) = CRSS_{SSH}\left[1-\left(\frac{kT}{\Delta E_b}\ln\frac{\dot{\varepsilon}_0}{\dot{\varepsilon}}\right)^{\frac{2}{3}}\right] \tag{D3}$$

where $\dot{\varepsilon}_0 = 10^4\ s^{-1}$ is reference strain-rate, $\dot{\varepsilon} = 5\ \times 10^{-5}\ s^{-1}$ the applied strain-rate for $Ni_{33.3}Co_{66.7}$ used in the experiment (Chowdhury et al., 2015), and ΔE_b the energy barrier for thermal activation which is defined as,

$$\Delta E_b = A_E\left(\frac{\Gamma}{b_F^2}\right)^{\frac{1}{3}} b_F^3\left(\mu_{avg}^V\frac{1+\nu_{avg}^V}{1-\nu_{avg}^V}\right)^{\frac{2}{3}}\left(\frac{\sum c_n\Delta\overline{V}_n^2}{b_F^6}\right)^{\frac{1}{3}} \tag{D4}$$

and the assumption of $\xi/b_F = 1.5$ results in the pre-factor A_E is 1.5618 and A_τ is 0.01785. The resulting SSH value (5.2 MPa) underestimates the experimental value (15 MPa)- see Table D1.

In summary, we showed that the $\xi/b_F = 1.5$ assumption does not hold for a wide range of FCC materials in Appendix C. The core-width ξ/b_F cannot be assumed and must be derived from energy minimization which was undertaken in the main text. We also showed that the SSH predictions in Table D1 underestimate the CRSS for the four benchmark FCC alloys (including the negative SFE cases) in comparison with lattice resistance calculations given in Tables 1 and B1.

References

Abuzaid, W., Patriarca, L., 2020. A study on slip activation for a coarse-grained and single crystalline CoCrNi medium entropy alloy. Intermetallics 117, 106682.

Abuzaid, W., Sehitoglu, H., 2017. Critical resolved shear stress for slip and twin nucleation in single crystalline FeNiCoCrMn high entropy alloy. Mater. Charact. 129, 288–299.

Alkan, S., Ojha, A., Sehitoglu, H., 2018a. Determination of latent hardening response for FeNiCoCrMn for twin-twin interactions. Acta Mater. 147, 149–164.

Alkan, S., Sehitoglu, H., 2019. Prediction of transformation stresses in NiTi shape memory alloy. Acta Mater. 175, 182–195.

Alkan, S., Wu, Y., Ojha, A., Sehitoglu, H., 2018b. Transformation stress of shape memory alloy CuZnAl: non-Schmid behavior. Acta Mater. 149, 220–234.

Barnett, D.M., Lothe, J., 1974. An image force theorem for dislocations in anisotropic bicrystals. J. Phys. F Met. Phys. 4, 1618–1635.

Cai, W., Arsenlis, A., Weinberger, C.R., Bulatov, V.V., 2006. A non-singular continuum theory of dislocations. J. Mech. Phys. Solids 54, 561–587.

Celebi, O.K., Mohammed, A.S.K., Krogstad, J.A., Sehitoglu, H., 2022. Evolving dislocation cores at twin boundaries: theory of CRSS elevation. Int. J. Plast. 148, 103141.

Celebi, O.K., Mohammed, A.S.K., Sehitoglu, H., 2023. Effect of Dislocation Character on the CRSS. Acta Mater. 254, 118982.

Chandran, M., Sondhi, S.K., 2011. First-principle calculation of stacking fault energies in Ni and Ni-Co alloy. J. Appl. Phys. 109, 103525.

Chowdhury, P., Sehitoglu, H., 2017a. Deformation physics of shape memory alloys – fundamentals at atomistic frontier. Prog. Mater Sci. 88, 49–88.

Chowdhury, P., Sehitoglu, H., 2017b. A revisit to atomistic rationale for slip in shape memory alloys. Prog. Mater Sci. 85, 1–42.

Chowdhury, P., Sehitoglu, H., Abuzaid, W., Maier, H.J., 2015. Mechanical response of low stacking fault energy Co–Ni alloys – continuum, mesoscopic and atomic level treatments. Int. J. Plast. 71, 32–61.

Cohen, J.B., Fine, M.E., 1962. Some aspects of short-range order. J. Phys. Radium 23, 749–762.

Curtze, S., Kuokkala, V.T., Oikari, A., Talonen, J., Hänninen, H., 2011. Thermodynamic modeling of the stacking fault energy of austenitic steels. Acta Mater. 59, 1068–1076.

Datta, A., Waghmare, U.V., Ramamurty, U., 2009. Density functional theory study on stacking faults and twinning in Ni nanofilms. Scr. Mater. 60, 124–127.

de Koning, M., Antonelli, A., Bazant, M.Z., Kaxiras, E., Justo, J.F., 1998. Finite-temperature molecular-dynamics study of unstable stacking fault free energies in silicon. Phys. Rev. B 58, 12555–12558.

Ding, J., Yu, Q., Asta, M., Ritchie, R.O., 2018. Tunable stacking fault energies by tailoring local chemical order in CrCoNi medium-entropy alloys. Proc. Natl. Acad. Sci. 115, 8919–8924.

Hirth, J.P., Lothe, J., 1992. Theory of Dislocations, 2nd Ed. Krieger Pub. Co., Malabar, FL.

Huang, H., Li, X., Dong, Z., Li, W., Huang, S., Meng, D., Lai, X., Liu, T., Zhu, S., Vitos, L., 2018. Critical stress for twinning nucleation in CrCoNi-based medium and high entropy alloys. Acta Mater. 149, 388–396.

Hull, D., Bacon, D.J., 2001. Introduction to Dislocations, 4th ed. Butterworth-Heinemann, Oxford [Oxfordshire].

Joós, B., Duesbery, M.S., 1997. The Peierls stress of dislocations: an analytic formula. Phys. Rev. Lett. 78, 266–269.

Kibey, S., Liu, J.B., Johnson, D.D., Sehitoglu, H., 2006. Effect of nitrogen on generalized stacking fault energy and stacking fault widths in high nitrogen steels. Acta Mater. 54, 2991–3001.

Kibey, S., Liu, J.B., Johnson, D.D., Sehitoglu, H., 2007. Predicting twinning stress in fcc metals: linking twin-energy pathways to twin nucleation. Acta Mater. 55, 6843–6851.

Labusch, R., 1970. A statistical theory of solid solution hardening. Phys. Status Solidi B 41, 659–669.

Laplanche, G., Kostka, A., Reinhart, C., Hunfeld, J., Eggeler, G., George, E.P., 2017. Reasons for the superior mechanical properties of medium-entropy CrCoNi compared to high-entropy CrMnFeCoNi. Acta Mater. 128, 292–303.

Laplanche, G., Schneider, M., Scholz, F., Frenzel, J., Eggeler, G., Schreuer, J., 2020. Processing of a single-crystalline CrCoNi medium-entropy alloy and evolution of its thermal expansion and elastic stiffness coefficients with temperature. Scr. Mater. 177, 44–48.

LaRosa, C.R., Ghazisaeidi, M., 2022. A "local" stacking fault energy model for concentrated alloys. Acta Mater. 238, 118165.

Li, X., Schönecker, S., Vitos, L., Li, X., 2022. Generalized stacking faults energies of face-centered cubic high-entropy alloys: a first-principles study. Intermetallics 145, 107556.

Liu, S.F., Wu, Y., Wang, H.T., He, J.Y., Liu, J.B., Chen, C.X., Liu, X.J., Wang, H., Lu, Z.P., 2018. Stacking fault energy of face-centered-cubic high entropy alloys. Intermetallics 93, 269–273.

Liu, S.F., Wu, Y., Wang, H.T., Lin, W.T., Shang, Y.Y., Liu, J.B., An, K., Liu, X.J., Wang, H., Lu, Z.P., 2019. Transformation-reinforced high-entropy alloys with superior mechanical properties via tailoring stacking fault energy. J. Alloys Compd. 792, 444–455.

Lu, S., Sun, X., Tian, Y., An, X., Li, W., Chen, Y., Zhang, H., Vitos, L., 2023. Theory of transformation-mediated twinning. PNAS Nexus 2, pgac282.
Mohammed, A.S.K., Celebi, O.K., Sehitoglu, H., 2022. Critical stress prediction upon accurate dislocation core description. Acta Mater. 233, 117989.
Nabarro, F.R.N., 1947. Dislocations in a simple cubic lattice. Proc. Phys. Soc. 59, 256–272.
Nabarro, F.R.N., 1967. Theory of Crystal Dislocations. Clarendon P., Oxford.
Nag, S., Varvenne, C., Curtin, W.A., 2020. Solute-strengthening in elastically anisotropic fcc alloys. modelling and simulation in. Mater. Sci. Eng. 28, 025007.
Nishizawa, T., Ishida, K., 1983. The Co−Ni (Cobalt-Nickel) system. Bull. Alloy Ph. Diagr. 4, 390–395.
Niu, C., LaRosa, C.R., Miao, J., Mills, M.J., Ghazisaeidi, M., 2018. Magnetically-driven phase transformation strengthening in high entropy alloys. Nat. Commun. 9, 1363.
Niu, C., Zaddach, A.J., Koch, C.C., Irving, D.L., 2016. First principles exploration of near-equiatomic NiFeCrCo high entropy alloys. J. Alloys Compd. 672, 510–520.
Ogata, S., Li, J., Yip, S., 2002. Ideal pure shear strength of aluminum and copper. Science 298, 807–811.
Okamoto, N.L., Fujimoto, S., Kambara, Y., Kawamura, M., Chen, Z.M.T., Matsunoshita, H., Tanaka, K., Inui, H., George, E.P., 2016. Size effect, critical resolved shear stress, stacking fault energy, and solid solution strengthening in the CrMnFeCoNi high-entropy alloy. Sci. Rep. 6, 35863.
Olson, G.B., Cohen, M., 1976. A general mechanism of martensitic nucleation: part I. general concepts and the FCC → HCP transformation. Metall. Trans. A 7, 1897–1904.
Peierls, R., 1940. The size of a dislocation. Proc. Phys. Soc. 52, 34.
Phillips, R., 2001. Crystals, Defects and Microstructures: Modeling Across Scales. Cambridge University Press, Cambridge.
Picak, S., Liu, J., Hayrettin, C., Nasim, W., Canadinc, D., Xie, K., Chumlyakov, Y.I., Kireeva, I.V., Karaman, I., 2019. Anomalous work hardening behavior of $Fe_{40}Mn_{40}Cr_{10}Co_{10}$ high entropy alloy single crystals deformed by twinning and slip. Acta Mater. 181, 555–569.
Read, W.T., 1953. Dislocations in Crystals. McGraw-Hill, New York.
Shang, S.L., Wang, W.Y., Wang, Y., Du, Y., Zhang, J.X., Patel, A.D., Liu, Z.K., 2012. Temperature-dependent ideal strength and stacking fault energy of FCC Ni: a first-principles study of shear deformation. J. Phys. Condens. Matter 24, 155402.
Shih, M., Miao, J., Mills, M., Ghazisaeidi, M., 2021. Stacking fault energy in concentrated alloys. Nat. Commun. 12, 3590.
Siegel, D.J., 2005. Generalized stacking fault energies, ductilities, and twinnabilities of Ni and selected Ni alloys. Appl. Phys. Lett. 87, 121901.
Stroh, A.N., 1958. Dislocations and cracks in anisotropic elasticity. the philosophical magazine. J. Theor. Exp. Appl. Phys. 3, 625–646.
Sun, X., Lu, S., Xie, R., An, X., Li, W., Zhang, T., Liang, C., Ding, X., Wang, Y., Zhang, H., Vitos, L., 2021. Can experiment determine the stacking fault energy of metastable alloys? Mater. Des. 199, 109396.
Tadmor, E.B., Miller, R.E., 2011. Modeling materials: continuum, Atomistic and Multiscale Techniques. Cambridge University Press.
Tian, L.Y., Lizárraga, R., Larsson, H., Holmström, E., Vitos, L., 2017. A first principles study of the stacking fault energies for FCC Co-based binary alloys. Acta Mater. 136, 215–223.
Togo, A., Tanaka, I., 2015. First principles phonon calculations in materials science. Scr. Mater. 108, 1–5.
van de Walle, A., Tiwary, P., de Jong, M., Olmsted, D.L., Asta, M., Dick, A., Shin, D., Wang, Y., Chen, L.Q., Liu, Z.K., 2013. Efficient stochastic generation of special quasirandom structures. CALPHAD 42, 13–18.
Varvenne, C., Luque, A., Curtin, W.A., 2016. Theory of strengthening in FCC high entropy alloys. Acta Mater. 118, 164–176.
Vítek, V., 1968. Intrinsic stacking faults in body-centred cubic crystals. the philosophical magazine. J. Theor. Exp. Appl. Phys. 18, 773–786.
Wang, J., Sehitoglu, H., 2013. Twinning stress in shape memory alloys: theory and experiments. Acta Mater. 61, 6790–6801.
Wang, X.X., Niu, L.L., Wang, S., 2018a. Energetics analysis of interstitial loops in single-phase concentrated solid-solution alloys. J. Nucl. Mater. 501, 94–103.
Wang, Y., Liu, B., Yan, K., Wang, M., Kabra, S., Chiu, Y.L., Dye, D., Lee, P.D., Liu, Y., Cai, B., 2018b. Probing deformation mechanisms of a FeCoCrNi high-entropy alloy at 293 and 77 K using in situ neutron diffraction. Acta Mater. 154, 79–89.
Wei, S., Tasan, C.C., 2020. Deformation faulting in a metastable CoCrNiW complex concentrated alloy: a case of negative intrinsic stacking fault energy? Acta Mater. 200, 992–1007.
Werner, K.V., Niessen, F., Li, W., Lu, S., Vitos, L., Villa, M., Somers, M.A.J., 2023. Reconciling experimental and theoretical stacking fault energies in face-centered cubic materials with the experimental twinning stress. Materialia 27, 101708.
Werner, K.V., Niessen, F., Villa, M., Somers, M.A.J., 2021. Experimental validation of negative stacking fault energies in metastable face-centered cubic materials. Appl. Phys. Lett. 119, 141902.
Wirth, L.J., Woodward, C., Farajian, A.A., 2022. Ab initio molecular dynamics of pipe diffusion in FCC Ni beyond transition state theory. Acta Mater. 222, 117357.
Wu, Z., Gao, Y.F., Bei, H., 2015. Single crystal plastic behavior of a single-phase, face-center-cubic-structured, equiatomic FeNiCrCo alloy. Scr. Mater. 109, 108–112.
Yin, B., Yoshida, S., Tsuji, N., Curtin, W.A., 2020. Yield strength and misfit volumes of NiCoCr and implications for short-range-order. Nat. Commun. 11, 2507.
You, D., Celebi, O.K., Mohammed, A.S.K., Abueidda, D.W., Koric, S., Sehitoglu, H., 2023. CRSS determination combining ab-initio framework and surrogate neural networks. Int. J. Plast. 162, 103524.
Zaddach, A.J., Niu, C., Koch, C.C., Irving, D.L., 2013. Mechanical properties and stacking fault energies of NiFeCrCoMn high-entropy alloy. JOM 65, 1780–1789.
Zhang, R., Zhao, S., Ding, J., Chong, Y., Jia, T., Ophus, C., Asta, M., Ritchie, R.O., Minor, A.M., 2020. Short-range order and its impact on the CrCoNi medium-entropy alloy. Nature 581, 283–287.
Zhang, S., Wang, G., 2022. Predicting mechanical properties of high entropy alloys with face centered cubic structure from first principles calculations. Mater. Today Commun. 32, 104059.
Zhang, Y.H., Zhuang, Y., Hu, A., Kai, J.J., Liu, C.T., 2017a. The origin of negative stacking fault energies and nano-twin formation in face-centered cubic high entropy alloys. Scr. Mater. 130, 96–99.
Zhang, Z., Sheng, H., Wang, Z., Gludovatz, B., Zhang, Z., George, E.P., Yu, Q., Mao, S.X., Ritchie, R.O., 2017b. Dislocation mechanisms and 3D twin architectures generate exceptional strength-ductility-toughness combination in CrCoNi medium-entropy alloy. Nat. Commun. 8, 14390.
Zhao, S., Osetsky, Y., Stocks, G.M., Zhang, Y., 2019. Local-environment dependence of stacking fault energies in concentrated solid-solution alloys. npj Comput. Mater. 5, 13.
Zhao, S., Stocks, G.M., Zhang, Y., 2017. Stacking fault energies of face-centered cubic concentrated solid solution alloys. Acta Mater. 134, 334–345.